Highlights

Experiments on the Breakup and Evaporation of Small Droplets at High Weber Number

Vasco Duke-Walker,Benjamin J.Musick,Jacob A. McFarland

- Droplet breakup experiments for small evaporating drops at high Weber number.
- Child droplet cloud length is determined by child droplet sizes and lag distances.
- Large child droplets predicted by the Rayleigh-Taylor instability drive cloud length.
- Child droplets evaporate in isolation without particle-particle vapor effects.

Experiments on the Breakup and Evaporation of Small Droplets at High Weber Number

Vasco Duke-Walker[a], Benjamin J.Musick[a] and Jacob A. McFarland[a]

[a]Mechanical Engineering, Texas A&M University, College Station, 77840, TX, USA

ARTICLE INFO

Keywords:
Breakup
Evaporation
Deformation
Parent Droplet
Child Droplet
Droplet Cloud

ABSTRACT

-Shock-driven multiphase mixing is present in numerous physical systems such as detonation-driven propulsion engines, liquid-vapor cloud explosions, and hypersonic flight droplet impacts. At the microscale, droplets experience deformation, breakup, and evaporation under extreme conditions (high Weber and Reynolds regimes). For small droplets, these phenomena are simultaneous and highly transient, making their interactions and interdependencies warrant further investigation. In this study, experiments are conducted in a shock tube facility to investigate these simultaneous droplet-scale phenomena. An interface consisting of small acetone droplets ($\varnothing$ 10-40 [μm]) is impulsively accelerated by a strong planar shock wave (Mach $\sim$ 2.09). The droplet size distribution is well-characterized *in-situ* utilizing a Phase Doppler Particle Analyzer (PDPA) and shadowgraphy. The development of child droplet clouds is captured through an ensemble of Mie scattering images. A simplified model is developed to interpret the experimental results, combining deformation, breakup, and evaporation models. The results indicate that the breakup of small droplets at high Weber numbers is likely dominated by the Rayleigh-Taylor (RT) mechanism, aligning with previous empirical models for low Weber numbers.

<tnote number>

1. Introduction

Many extreme environments exist where droplets will encounter high-speed impulsive acceleration resulting in droplet deformation, breakup, and evaporation due to aerodynamic forces and strong temperature gradients. Such environments can be as varied as droplet impact on hypersonic flight vehicles, blast and detonation mitigation in process safety, explosive dispersal of chemical compounds, and high-speed combustion in detonation-cycle engines. In order to model and thoroughly understand the relevant physics of an evolving droplet, an understanding of the broader field of shock-driven multiphase mixing is needed, from the cloud-scale (macroscale) down to the individual droplet dynamics (microscale). In this discussion, note that the term particle is used when referring to physics applicable to any discrete phase, while the term droplet is used when discussing physics unique to liquid particles.

Shock-driven multiphase mixing can be divided into two regimes: the macroscale (motions of droplet groups) and the microscale (individual droplets). On the macroscale, the evolution of multiphase fluid mixture interfaces is considered in the SDMI, including hydrodynamic mixing, vorticity deposition, and particle lag effects (velocity equilibration time). Further, evaporation can be limited by large-scale mixing of the particle and vapor phase, introducing particles to new dry gas. More importantly, understanding the macroscale can be further improved by exploring critical physical phenomena on the microscale, such as breakup and evaporation, which drive the behaviors at larger scales. Breakup and evaporation are relevant because they alter particle response times and limit vapor mixing rates.

High-speed single droplet breakup has mostly been considered without evaporation; however, as the size of the droplets becomes smaller, evaporation becomes more dominant. Goossens, Cleijne, Smolders and Van Dongen (1988) studied experimentally shock strength effects on evaporation with small stable water droplets, $0.5 < d_p < 2[\mu m]$, showing good agreement with simple evaporation models. Paudel, Dahal and McFarland (2018) performed full 3D simulations at Mach 1.65 and droplet size $d_p < 10[\mu m]$, and showed disparities in the case of evaporating and non-evaporating droplets. Paudel et al. (2018) suggested that evaporation and droplet size play a strong role in the hydrodynamic development of the SDMI, with time scales for momentum equilibration and evaporation being strongly dependent on droplet size. It was observed that large droplets start to lag behind the flow, inducing small-scale perturbations and reducing hydrodynamic growth. In contrast, small droplets would equilibrate and evaporate quickly, producing more classic Richtmyer-Meshkov instability (RMI) behavior Dahal and McFarland (2017); Black, Denissen and McFarland (2017). These were further investigated and presented experimentally at Mach 1.65, and $2 < d_p < 11[\mu m]$ by Middlebrooks et al. (2019), in which a second droplet breakup event occurred at re-shock (second acceleration by reflected shock wave), evaporating the droplets nearly instantaneously. Further experimental work by Duke-Walker, Allen, Maxon and McFarland (2020) was performed to understand the coupled effect on droplet breakup and evaporation using acetone droplets at Mach 1.65 and $d_p = 10[\mu m]$. This work showed

<tnote text>
*Jacob A. McFarland
vascoduke@tamu.edu (V. Duke-Walker)
https://fmecl.engr.tamu.edu (V. Duke-Walker)
ORCID(s):

that droplet breakup contributed significantly to the evaporation process at early time; however, evaporation was limited by hydrodynamic mixing at late times.

At the microscale, small droplets subjected to sudden acceleration from a shock will experience aerodynamic forces leading to droplet deformation, breakup, and finally evaporation. The Momentum equilibration rate, which is the rate at which particles adjust to changes in the flow field velocity, is the most significant factor affecting macroscale shock-driven multiphase mixing and is primarily controlled by breakup rates and final child droplet sizes.

Droplet breakup phenomena are divided into various regimes described by the Weber number, $We = \rho_g v_{pg}^2 d_p/\sigma$, the ratio of inertial to surface tension effects, Reynold's number, $Re = \rho_g d_p v_{pg}/\mu$, inertial to viscous effects, and Ohnesorge number, $Oh = \mu/\sqrt{\rho\sigma d_p}$, relating viscous to inertial and surface tensions forces. Here ρ_g is the density of the gas, $v_{pg} = |v_g - v_p|$ the relative droplet to gas velocity, d_p the initial parent droplet diameter, and σ the surface tension of the liquid droplet. The critical Weber number is determined when $Oh < 0.1$ from $We_c = 12 \cdot (1 + Oh^{1.6})$ from Pilch and Erdman (1987), indicating that breakup will occur for low viscosity fluids at a $We \sim 12$. At low We, various breakup regimes exist that result from the combination of Rayleigh-Taylor and capillary instabilities Kirar, Soni, Kolhe and Sahu (2022). For the flow conditions considered in this paper, the droplet breakup process is expected to be in the high We, shear stripping or catastrophic regimes, depending on the reference source for breakup regimes.

Several empirical models have been analyzed for low We in the bag and bag and stamen breakup regimes, providing accurate results of the breakup time and the representative Sauter mean diameter of the child droplets (Hsiang and Faeth, 1992; Wert, 1995). Hsiang and Faeth (1992) proposed that child droplet sizes are based on the growth of the liquid boundary layer thickness. Their proposed size correlation is valid for $We < 10^3$ and $Oh < 0.1$. Wert (1995) proposed a model based on linear stability theory for capillary waves in the toroidal ring of the bag breakup regime, tuned with experimental data from Hsiang and Faeth (1992) for large droplets $d_p > 500[\mu m]$. Furthermore, the same breakup model (Wert, 1995), was tuned by Duke-Walker et al. (Duke-Walker, Maxon, Almuhna and McFarland, 2021) in simulation efforts to match experimental data for small droplet $d_p = 10[\mu m]$ at moderate Mach numbers (Mach 1.65) (Middlebrooks et al., 2019). A review of previous breakup models applied to similar experiments as those presented here can be found in Duke-Walker et al. (2021).

Theoretical breakup models (e.g. TAB and KHRT) have provided a deeper understanding of the deformation process and hydrodynamic instabilities occurring on the droplet surface. The TAB model has been shown to greatly underpredict the mean drop size after breakup for a jet (Tanner, 1997) and shock-driven droplets (Duke-Walker et al., 2021), while the ETAB model (Tanner, 1997) produces droplet sizes much larger than experiments show for low We. Thus, the TAB and ETAB models were not considered in this work. The KHRT model has been advanced by various authors (Liu, Mather and Reitz, 1993; Beale and Reitz, 1999), describing the breakup process through the Kelvin-Helmholtz (KH) and Rayleigh-Taylor (RT) instabilities. The model estimates the most unstable, fastest growing wavelengths, Λ, and respective growth rate, Ω, for each mechanism to determine the breakup time and child droplet sizes.

Both KH and RT instabilities can occur simultaneously with the RT instability terminating the KH as seen here. In other cases, the KH instability finishes the breakup process before the RT breakup completes or the KH may be prevented altogether when its wavelength is too large relative to the parent droplet diameter (at low We). Generally, the RT mechanism is considered to dominate the breakup process at lower We, while the KH mechanism dominates at higher We Theofanous, Mitkin, Ng, Chang, Deng and Sushchikh (2012). The KHRT model has shown satisfactory results in predicting the child droplet sizes in the primary breakup of a diesel jet (Liu et al., 1993). Unfortunately, there are still some uncertainties in the model since it strongly depends on the choice of coefficients and must be tuned to experimental work, becoming an open challenge Sharma, Chandra, Basu and Kumar (2022).

Empirical and theoretical breakup models have been widely developed, tested, tuned, and reiterated to make their application more general for different breakup regimes. Studies such as Stefanitsis, Strotos, Nikolopoulos, Kakaras and Gavaises (2019) show how different experimental conditions may require a different application of zero-dimensional models or coefficients for good numerical replication of the deformation process. Full 3D simulations of droplet breakup are non-trivial tasks requiring modeling aspects that make their validity difficult to determine. However, studies attempting to match experimental conditions using Euler Meng and Colonius (2018) or coupled Euler-Lagrange methods Stefanitsis, Koukouvinis, Nikolopoulos and Gavaises (2021) have shown relatively good agreement with their respective study.

Notably, many previous experiments have been for relatively larger droplets (order of millimeters). Widdecke, Klenk and Frohn (1995) conducted a study with isopropanol droplets with 50-200 $[\mu m]$ diameters at shock Mach numbers of 2-6, with $We \sim 10^4$ and $Re \sim 10^4$, observing breakup and cloud formation, however, no efforts were made towards modeling the phenomena. Kobiera, Szymczyk, Wolański and Kuhl (2009) performed similar studies with hexane droplets of $0.6 - 2.0$ [mm] in diameter at $We \sim 10^3 - 10^5$ and $Re \sim 10^4 - 10^5$, subjected to shocks strength $M = 2, 2.9$. It was observed that the time for acceleration and dispersion of a droplet into a cloud was dependent on the diameter and incident shock strength, with the dispersed cloud diameter being We dependent and dispersion time a function of droplet size. Park, Yeom, Hong and Moon (2017) studied water droplets with diameters of 2.0-3.6 [mm] at shock wave Mach numbers of 1.4-2.2, producing $We \sim 10^3 - 10^4$, and $Re \sim 10^4$. This work observed a deficiency in predicted droplet acceleration by

the available models. It is worthwhile to note that, in the studies surveyed, little attention was given to small droplets $d < 50[\mu m]$ under similar We regimes.

In this study, a series of shock-droplet experiments were undertaken with relatively small droplet sizes ($10 - 40[\mu m]$) to provide insight into the coupled behavior of the shock-droplet breakup and evaporation. As stated previously, droplet breakup for large droplets has been considered mostly without evaporation. However, evaporation becomes significant as the droplet size is made smaller. The experiments conducted here provide metrics of droplet cloud development at various post-shock times, from shock interaction to droplet extinction. Laser Mie scattering and Planar Laser Induced Fluorescence (PLIF) imagery were utilized to track the development of the liquid and vapor species of acetone, respectively. Special attention was placed on creating an interface that would be insensitive to mixing and a thorough characterization of the initial conditions was conducted, specifically the distribution of droplet sizes in the interface. Several existing models are considered, and their predictions are compared to experimental data. Additional data points were drawn from published data Kobiera et al. (2009) for comparison to model predictions. A simple model for concurrent breakup and evaporation that most accurately predicts the experimental results is thus proposed.

2. Experimental Facility

The following section will familiarize the reader with the equipment used to conduct the experiments reported in this article, namely the shock tube facility, diagnostics, data acquisition system, and the particle-gas curtain shaping device.

2.1. Shock Tube Facility

Experiments were conducted in the fluids mixing shock tube facility shown in figure 1. The shock tube is divided into three main sections: a driver (high-pressure), driven (low-pressure), and test section housing the interface and diagnostics. A 24 gauge (0.51 [mm]) galvanized steel sheet-metal diaphragm is placed between the driver and driven sections and the two sections are clamped together with two 50 kip dual actuating hydraulic rams, sealing the system. The hydraulic clamping mechanism allows for quick turnaround time (under 60 [s] to replace diaphragms) as well as the ability to use diaphragms sufficiently strong enough to obtain shock strengths up to Mach 2.75. The driver section is pressurized to just below the diaphragm breaking pressure, and the experiment is initiated by a pulse of high-pressure gas, at which point the diaphragm is instantaneously ruptured by an x-shaped knife. This method has proved to provide repeatable and reliable experiments. The driven section is long enough to allow for a stable planar shock to fully develop before reaching the test section at atmospheric conditions. The test section is equipped with multiple acrylic windows that were positioned to visualize the droplet field from the sides and above. The laser beam enters through a Sapphire window positioned in the end wall of the test section.

2.2. Diagnostics and Data Acquisition

The firing sequence and signals are automated through a LabVIEW code and NI data acquisition hardware acquiring dynamic data at 1 [MHz]. Two dynamic pressure transducers are utilized to measure the shock velocity from the recorded pressure jump times, and used for timing of the trigger signals to the diagnostics in the test section. The laser pulses and synchronized camera imaging are initiated by the Insight 4G program at a precise time after the shock passes, as measured by the pressure transducer trigger signal. A Litron NanoPIV 200 laser is utilized, providing 200 [mJ] and 40 [mJ] of laser energy at 532 [nm] and 266 [nm] wavelengths, respectively. The laser output is focused with a plano-convex, concave lens and transformed into a sheet with a cylindrical lens. The cylindrical lens is rotated 90 degrees to allow for planar-imaging from any of the window ports in the test sections, as seen in figure 1, and 6.

Two 29 [MP] cameras were utilized to capture the morphological behavior of the gas and droplets. One camera was filtered to see only the fluorescence emission from acetone vapor excited by the 266 [nm] laser emissions, while the other was filtered to see only the 532 [nm] Mie-scattered light. Neutral density filters were applied to the camera receiving Mie-scattered light as needed to reduce overexposure. A Phase Doppler Particle Analyzer (PDPA) system from TSI inc. was used to measure droplet sizes *in-situ*, before shock initiation. This system used a continuous wave laser at 561 [nm] to measure droplet sizes via FlowSizer64 software. A high-speed shadowgraphy system was also implemented, consisting of an 880 [mW] LED white light source with collimating optics, a high-speed camera (Phantom T3610, resolution 1280x800, 8-bit pixel size 18 [um]), and a long-distance microscope (K2 Distamax) lens with a 44 [mm] extension tube.

Further details about the shock tube facility are provided in Duke-Walker et al. (2020).

2.3. Multiphase Interface Shaping Apparatus

In this work, the acetone droplets were generated using a focused ultrasonic (oscillating at 120 [kHz]) spray nozzle designed by Microspray Leiby (2021). This device has the advantage of being able to produce consistent droplet size with a low relative Span Factor (uniformity of the drop size distribution) and a low spray dispersion angle. This device generates droplets via periodic capillary waves induced in a liquid film on the flat nozzle tip. The waves are induced by a piezo-electric actuator at the base of the nozzle. The frequency at which the nozzle vibrates dictates the droplet diameter produced. The ultrasonic nozzle is driven by a broadband ultrasonic generator of a 20-watt tracking driver power and a 25-120 [kHz] output frequency range. The droplet median diameter of the nozzle can be estimated from ultrasonic atomizing theory Lang (1962), as $D_{0.5} = 0.34\frac{8\pi\sigma}{\rho_l f^2}$, in which, σ is the surface tension [N/m], ρ_l is the density of the liquid $[kg/m^3]$and f the operating frequency [Hz].

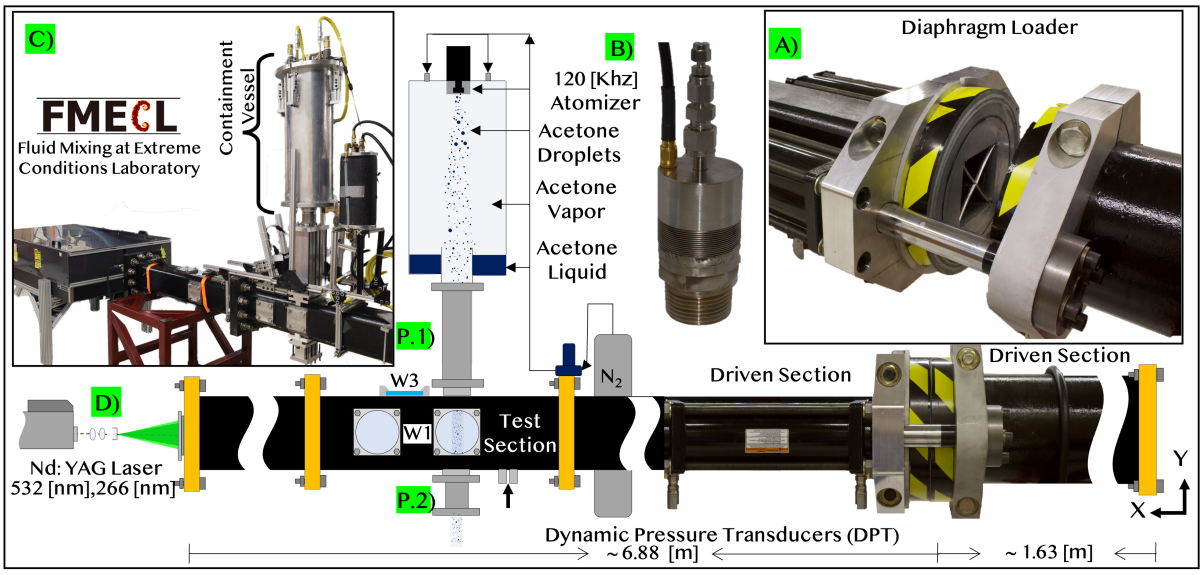

Figure 1: Experimental Facility. A) Hydraulic diaphragm loading mechanism. B) Ultrasonic atomizing nozzle. C) Test sections with laser table and aerosol containment vessel, D) Nd:Yag Laser 532[nm] and 266 [nm].

The acetone droplets were mixed into pre-saturated carrier gas (nitrogen gas saturated with acetone vapor) in a containment vessel shown in figure. 1 before flowing into the test section. A stable rectangular interface was achieved between the droplet-laden carrier gas and the surrounding test section gas via an interface shaping device (ISD). This device directs the droplet-laden gas into the test section in a controlled manner creating a stable rectangular interface at various flow concentrations. Compared to our previous work Duke-Walker et al. (2020); Middlebrooks et al. (2019), this device increases the cross-sectional interface area and delays any hydrodynamic mixing during the droplets' deformation, break up, and evaporation process. The ISD is composed of hollow rectangular aluminum housing 127[mm] x 50.8[mm] with inserts made of solid 3D-printed nylon. As shown in Balakumar, Orlicz, Tomkins and Prestridge (2008); Orlicz (2007), a dramatic improvement in the interface stability can be achieved by tuning the 3D flow-straightening geometry.

Two main flow stabilization sections were constructed to control the multiphase interface's shape and stabilization, one at the entrance (upstream flow stabilization P.1) and one at the exit (downstream flow stabilization P.2) of the test section (Figs. 4 - 1). The main goal of the upstream flow stabilization device is to shape and straighten the multiphase droplet-vapor-gas flow before entering the test section. It is composed of three subsections; a circular section to allow the flow to develop and smoothly transition, a honeycomb to straighten the incoming flow and reduce possible vortex growth, and a contraction to smoothly shape the interface. Similarly, the downstream flow stabilization device P.2 is composed of a secondary honeycomb and contraction, allowing for a smooth transition as the interface exits the tube. The downstream device also shields the curtain from any flow disturbances from the outside air. Design parameters for the honeycomb dimensions and contraction limitations designs were obtained from Mauro, Brusca, Lanzafame, Famoso, Galvagno and Messina (2017).

3. Experimental Methodology

This section expands on the methodologies and techniques utilized to characterize the multiphase droplet field, initial experimental conditions, and experimental variation.

3.1. Droplet Characterization

Acetone is an ideal fluid for studying droplet breakup and vaporization due to its thermophysical properties, which results in high We (low surface tension) with rapid evaporation (high vapor pressure). Acetone is also similar to fuels such as ethanol and methanol, having similar surface tension, density, and low viscosity ($Oh < 0.1$). Additionally, at the droplet sizes and shock conditions in this work, the thermophysical properties of acetone allow for similar evaporation and breakup mechanisms to those of fluids with lower vapor pressures and higher surface tensions at stronger shock conditions, such as ($C_{10} - C_{12}$) hydrocarbons in a detonation environment. Furthermore, acetone vapor pressure is high enough at standard pressure and temperature to produce concentrations sufficient to allow fluorescence imagery in atmospheric air. More detail on the behavior of acetone droplet-vapor-gas systems can be found in Duke-Walker et al. (2020).

The size distribution of acetone droplets produced was extensively characterized via two different measurement techniques, Phase Doppler Particle Analyzer (PDPA) and high-speed microscopy shadowgraph. The concurrent methodologies aided in reducing uncertainty in the size distribution,

both from the nozzle and inside the multiphase interface. The optical method compensated for the PDPA's limitations (volume and spatial resolution), while the PDPA compensated for diffraction-limits on measurable droplet sizes in the optical method, complementing each other well. The PDPA method, while having a limited measurement volume, is superior at resolving small droplet sizes when compared to current direct imaging methods such as shadowgraphy and digital in-line holography Guildenbecher, Gao, Chen and Sojka (2017).

3.1.1. Phase Doppler Particle Analyzer Measurements

The PDPA system provides an accurate and reliable droplet size distribution and droplet velocity TSI via the use of measured diffraction patterns from droplets illuminated by intersecting lasers. The PDPA system requires frequent and careful calibration since a slight misalignment of the laser beams could alter the phase measurements and size results. Because of this, an initial parametric study was conducted to determine the most accurate and efficient operating conditions for the device and measured conditions. The optimum beam intersection position was determined by obtaining a high data rate [Hz] and burst efficiency ($Br > 70[\%]$). Then a study of the photomultiplier tube (PMTs) voltage setting was performed to determine the best settings, based on the PDPA manual from TSI. The PMT transforms the scattered light and converts it to an electrical signal, where the PMT voltage increases its sensitivity. PMT voltage is one of the most critical parameters that effects the measurable particle sizes. As the PDPA system acquires data, the sizes measured will fluctuate over time (number of measurements) and the best settings are indicated when the variation in d_{10} is minimized. The study found that the optimum laser power was $10 - 30[\%]$, PMT voltage 425 [V], and Burst threshold 30[%]. Furthermore, the PDPA system was calibrated at the beginning of every experimental session and collected data analyzed against system intensity validation metrics (max diameter difference 10 [%], the slope of upper intensity curve 0.6 [$mV/\mu m^2$]), ensuring the validity of the measurements. A total of thirty measurements of the spray characterization were conducted outside and inside the shock tube test section to ensure that the droplet size distribution was well characterized and had no considerable variation. The total number of valid droplet size measurements collected *ex-situ* and *in-situ* were 828,475 and 32,307.

A representation of the setup utilized for collecting the statistical data can be seen in figure 4. The system was used *ex-situ* and *in-situ* with a refraction scatter angle of 32.5 degrees between the laser beam (PowerSight Module PS-TM-2D-R) and the Fiber Optic Transmitting Probes with a lens focal length lens of 70 [mm]. The laser was integrated with a lens of 300 [mm] focal length, allowing us to measure droplet diameters between 0.5 - 125 [μm].

3.1.2. High Speed Microscope Shadowgraphy

The high-speed microscope shadowgraphy setup was utilized to verify the measurements of the PDPA system.

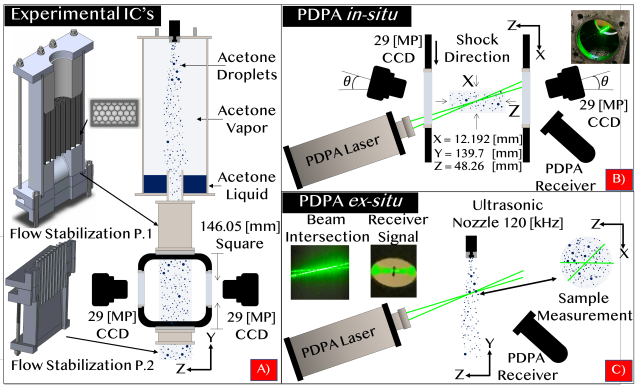

Figure 2: A) Multiphase droplet-gas curtain system, Phase Doppler Particle Analyzer (PDPA): B) Inside the shock tube test section and C) Outside free-handle sample

The shadowgraphy lens was set to produce a 7.25X magnification, with a pixel size of $\sim 2.5[\mu m]$ and the high-speed camera system was set to a 1 $[\mu s]$ exposure time. Calibration images at this magnification were captured with a target (R1L3S2P) with a 1 [mm] long scale with 10 $[\mu m]$ divisions with low reflectivity. A 532 [nm] (10 [nm] FWHM) filter was placed in front of the LED source to provide monochromatic illumination resulting in higher sensitivity and contrast as droplets passed through the illuminated region. A MATLAB routine was developed to identify individual droplets to create a statistical representation of the droplet size distribution.

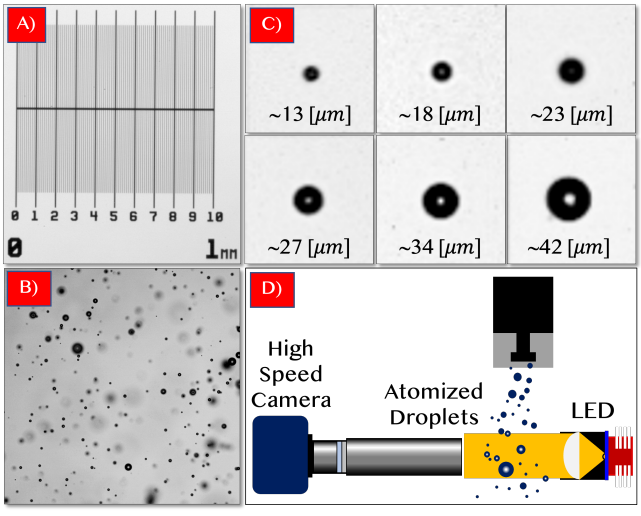

Figure 3: Microscopy shadowgraph: A) Calibration target, B) Example of the droplet field, C) Sample droplets diameter, D) System configuration

3.2. Initial Conditions

A thorough understanding of the initial conditions is necessary to validate and compare the performance of existing breakup and evaporation models. For this work, the focus was placed on controlling the multiphase interface, and characterizing the droplet and gas mixture. The shock tube was

initially filled with dry (no acetone vapor) atmospheric air at standard temperature and pressure (approximately 1 [atm] and 293 [K]). The multiphase interface fluid is composed of liquid acetone droplets and nitrogen gas saturated with acetone vapor (40.69 [%] by mass) at 1 [atm] and 293 [K]. The stability of the multiphase interface, droplet-gas curtain created by the ISD, was analyzed utilizing a time sequence Mie-scattering and PLIF images of the X-Y plane. Various gas flow rates were tested to find the most stable regime, and atomized liquid droplet flow rates adjusted accordingly. A combination of images of the curtain on the X-Z and X-Y planes were captured and post-processed to quantify the interface shape. These measurements showed that the rectangular shape measured to be a width of $X \sim 12.19$ [mm], length of $Z \sim 48.26$ [mm], and height of $Y \sim 139.7$[mm], as can be seen in figure. 4.

Concentration and statistical droplet size distribution measurements were collected and analyzed to validate the multiphase curtain characteristics. For this work, the droplet concentration was controlled via liquid mass flow rate, set by a syringe pump at $\sim 1.5[\frac{ml}{min}]$ and gas mass flow rate, set via mass controller to $\sim 10[SLM]$. The droplet concentration was measured via a filtration retention device Duke-Walker et al. (2020) and the mixture was found to be 99.99% by volume gas, leaving $< 0.01\%$ for the droplet field, indicating negligible droplet-to-droplet interactions in the initial conditions.

The statistical size distribution of droplets *ex-situ* and *in-situ* was measured with PDPA and shadowgraphy (as detailed in section 3.1.1 and 3.1.2) to be compared with theoretical droplet size predictions based on acoustic theory as shown in section 2.3. Taking the droplet median diameter from theory as $d_{0.5} = 13.02[\mu m]$, PDPA measurements *ex-situ* showed $d_{0.5} = 12.05[\mu m]$ and *in-situ* $d_{0.5} = 13.9293[\mu m]$, while shadowgraphy *ex-situ* found $d_{0.5} = 17.92[\mu m]$. PDPA results and theory showed excellent agreement. The shadowgraph numerically disagreed; however, it is understandable since it is limited to measuring droplets larger than 12.5 $[\mu m]$ for the current setup, which is the bulk of droplets within the distribution. When the shadowgraphy droplet size probability distribution was scaled to show similar probability above the detectable diameter, it showed excellent agreement with the PDPA data sample, as seen in figure. 5.

While PDPA accuracy and sample rate are high, it is limited by the maximum droplet size detected with the lens and sampling volume of our current configuration. The sample volume of the shadowgraphy system is higher than the PDPA system and allowed for measurement of larger droplets, though the sample rate was lower and limited at small droplet sizes by diffraction. Finally, the shadowgraph showed that droplet diameters beyond $d > 125[\mu m]$ do not play a significant role, which is the maximum droplet diameter that the PDPA can detect with the currently equipped lens.

The size statistics of the droplets, which are considered the initial conditions in our modeling section, are taken to be

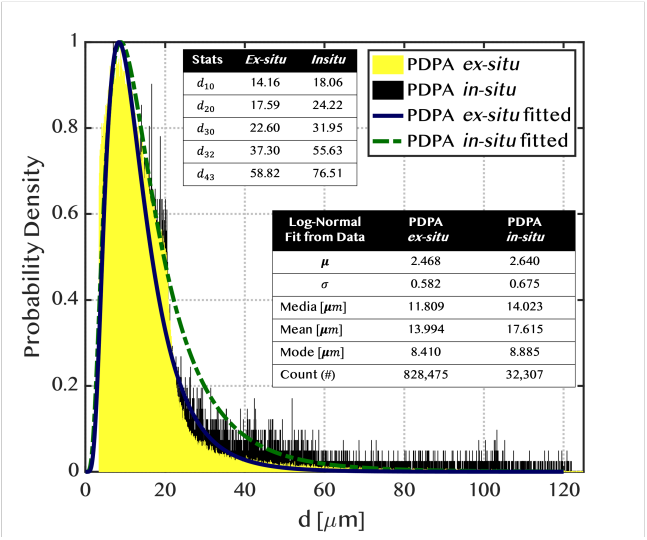

Figure 4: Phase Doppler Particle Analyzer (PDPA) outside and inside the shock tube test section

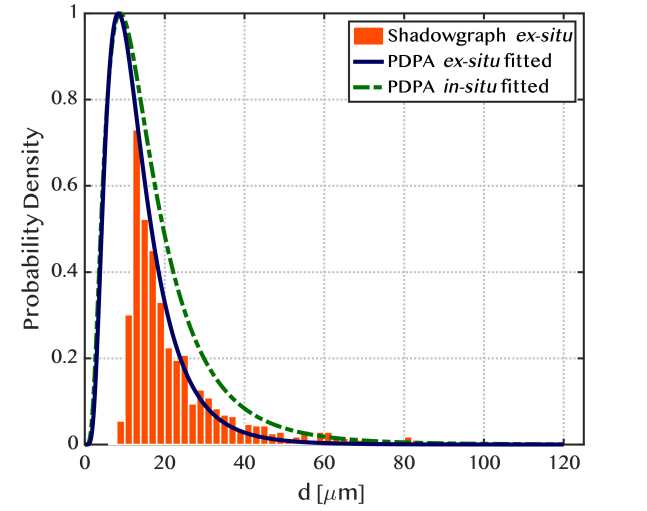

Figure 5: Shadowgraph outside, PDPA outside and inside the shock tube test section

those of the *ex-situ* PDPA data, $d_{10} = 14.16[\mu m]$ and $d_{32} = 37.3[\mu m]$, as these have the highest statistical confidence. The statistical droplet distribution from the PDPA can be seen in figure.4.

3.3. Experimental Diagnostics

Before every experiment, the laser alignment and its optics in conjunction with the camera lens must be checked and secured, and all-optical equipment and windows must be cleaned to guarantee optimal performance. A calibration target is positioned at the center of the test section window to indicate the center of the interface with respect to the cameras. An example is shown in figure 6. Once the optical system is ready, calibration and background images are acquired to account for the changes in the experimental setup as cameras get re-positioned. The camera focus is set at the

Table 1
Experimental camera setting

t [μs]	0 - 25	0 - 125	125 - 300
Aperture	22	16	5.6 - 2.8
Filter [nm]	532	-	-
Neutral Density	4	-	-

mid-range of the hyper-focal distance and further adjusted to the droplet (Mie-scattering signal) or gas (fluorescence signal) field. The cameras, depending on the experimental times, as shown in table (1), were adjusted not to overexpose or over-saturate the CCD sensor. Three primary camera settings were utilized to account for the variation in scattered light intensity from the resulting breakup process, child droplet cloud growth, and evaporation, as shown in table 1.

For the first 0 - 25 [μs], the camera is set on window 1 (W1 in Figs 1 and 6), perpendicular to the shock tube at $\theta = 0$ with a 0.41X magnification, to capture droplets at their initial conditions and during early breakup times. Due to the excess scattered light during breakup, the camera aperture, and neutral density filters were adjusted accordingly, as presented in table (1). The second camera position, set for window 1 with $\theta = 45$ and a magnification of ~0.3X, allowed an experimental visualization from 0 - 125 [μs]; however, the highest quality images were obtained after 25 [μs]. This setting captured the initial conditions and droplet cloud growth. The cameras were inclined to extend the field of view and bridge the gap between windows. Lastly, the third camera position, at the top of the test section in window 3 (W3 in Figs 1 and 6) with a $\beta = 0$ and a magnification of ~0.3X, was selected to capture the late time evolution and evaporation of the child droplet cloud. Calibration images were captured for each camera setup, allowing droplet and gas field images to be overlaid, obtaining a ratio to transform from [pixel] to [mm], and providing an image map for correcting optical distortion due to camera inclination angle.

The oblique image projection was adjusted to correct for the camera inclination angle by following the transformation proposed by Loomis This method takes four cardinal points from the original calibration target to warp, transform, and remap the image plane. Once the distorted calibration images are corrected, the experimental images are rectified following the same approach, as seen in figure 6 C and D. These steps ensure that the experimental results will replicate the correct [pixel] to the [mm] ratio when detecting and calculating the actual size of the child droplet cloud, as will be demonstrated in section 4.2.

Having described all experimental equipment calibration and characterized the multiphase interface, we move now to the experimental procedures for initiating (firing) a shock wave. The firing procedures begin by replacing the diaphragm and filling the shock tube with clean ambient air. This must be performed to remove any residual acetone vapor from previous runs and eliminate dust or debris in

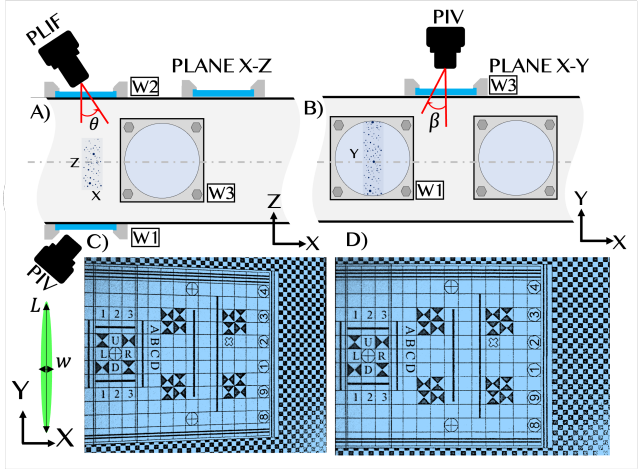

Figure 6: Angular Distortion: A) location 1 at two angles ($\beta = 0$ and $\beta = 45$) B) location 2 at the top of the window $\beta = 0$, C) original distorted image, and D) corrected distorted image

Table 2
Experimental Post-Shock Conditions and Breakup initial conditions

Mach	V [m/s]	P[kPa]	T [K]
2.09 ± 0.01	461.3 ± 4.6	493.6 ± 6.4	516.6 ± 3.2

Table 3
Breakup initial conditions

$d_p[\mu m]$	Oh	W_e	R_e
14.16	0.02	662 ± 19	1647 ± 21
37.3	0.01	1743 ± 49	4338 ± 56

the shock tube. An automatic shock firing sequence (ASFS) was developed with the LabVIEW control program, following the procedure described by Duke-Walker et al. (2020) with slight variations, to gain repeatability and reduce the procedure complexity. In the ASFS, the driver pressure was set to reach a target static pressure of 460 [psi] by filling slowly through a small solenoid valve. Once this pressure was reached, a large solenoid valve was actuated to raise the pressure quickly (within $\sim 1[s]$) to the diaphragm breaking pressure, approximately ~ 500 [psig]. The supply gas pressure was maintained within a gas tank at a pressure of 1000 [psig]. During the ASFS, the interface was introduced whenever the pressure in the driver reached 375 [psig], followed immediately by the carrier gas at 385 [psig]. This increase in the boost valve pressure allowed a reliable and instantaneous break of the diaphragm. The voltage threshold was set to 0.4 [V] inside LabVIEW ensuring that the dynamic pressure transducers (DPT) captured the shock and the timing was repeatable. Once the first DPT detects the shock, two laser pulses are triggered, capturing two frames (i.e., A B) on each camera. Frame A contains the initial droplet location just before shock interaction, and frame B shows the child droplet cloud development. These procedures were repeated for each experimental trial until the complete morphological interface development was obtained.

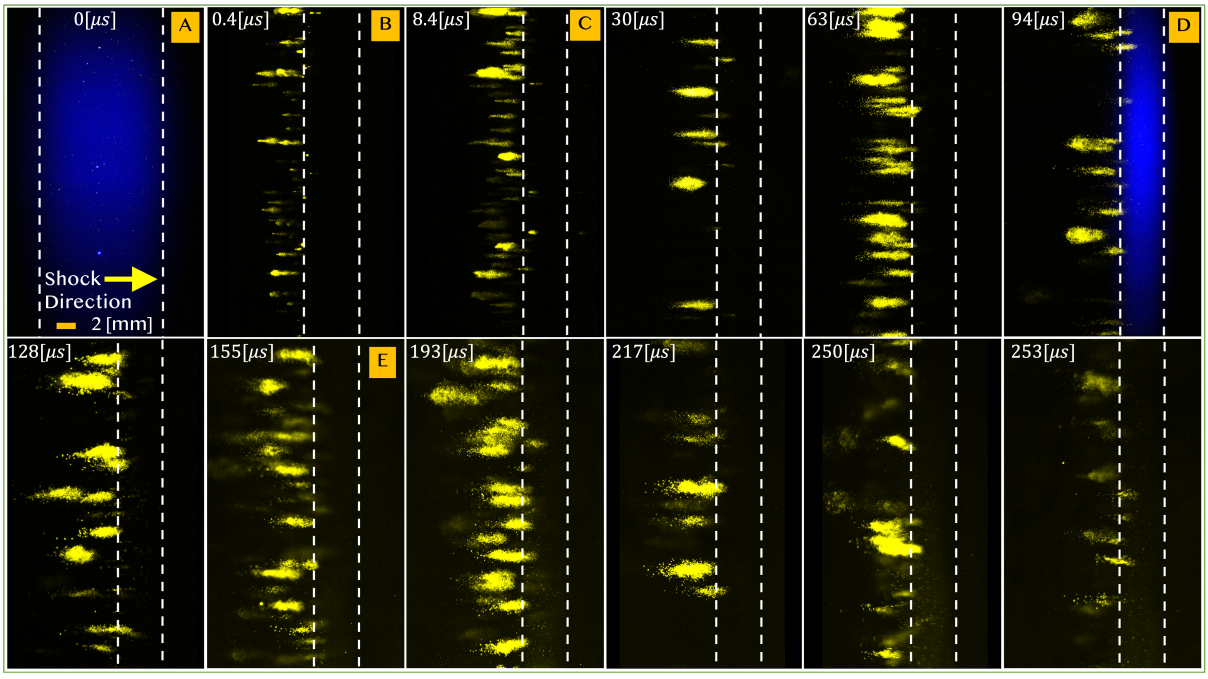

Figure 7: Time series ensemble images of experimental results: A) initial conditions prior shock arrival, B) droplet break up, C) onset of cloud growth, D) PLIF signal at a later time, E) cloud growth stagnation and evaporation Images captured from 0 - 125 [μs] were taken in plane X-Y and 125 - 300 [μs] in plane X-Z.

Another important factor to be considered in modeling the experimental results is the run-to-tun variation of the shock strength. One of the primary causes of this variation was found to be variations in the diaphragm; the deviation in thickness was up to $\pm 0.00075[in]$ from the nominal value of $0.025[in]$, enough to cause a variation in bursting pressure and shock strength between experiments. Other factors that could have contributed to the variations between experiments were dulling of the knife edge, and variation in metallurgical properties of the diaphragm. In practice, the shocks were still within a close range of Mach numbers, between 2.09 ± 0.01. At these Mach strengths, it can be estimated that the jump from atmospheric to post-shock conditions will vary in pressure, temperature, and velocity. as shown in **Table** 3.

4. Experimental Results

This section will discuss the experimental results from a qualitative and quantitative point of view, giving a more detailed insight into the temporal and morphological evolution of the multiphase interface.

4.1. Qualitative Description of Droplet Cloud Evolution and Evaporation

All experimental images have been corrected and converted from [px] to [mm] with their respective size calibration image. The droplet and gas contributions are overlaid to describe the droplet development qualitatively. The overlay was performed by taking four coordinate points from the corrected calibration image from both 29 [MP] cameras and applying them to the experimental images. For further details, the reader is encouraged to see Duke-Walker et al. (2020). Specifically, a MATLAB algorithm was implemented to provide a quantitative measurement of cloud growth, relative position, velocity, and trajectory and is detailed in section 4.2. Subsequently, once all experimental images were processed, a time series evolution of the particle cloud was assembled as shown in figure 7 and 9. Figure 7 shows the droplet field (Mie-scattered 532 [nm] light) in yellow, while the vapor field (laser-induced fluorescence) is shown in blue at $t = 0[\mu s]$. At all other times, $t = 0.4[\mu s]$ through $t = 253[\mu s]$, the X locations, upstream and downstream edges, of the vapor field are indicated by dashed white lines for clarity. The dotted lines represent the predicted location of the acetone vapor interface, based on 1D gas dynamics calculations. Images of acetone fluorescence are shown at two times to verify the position predicted by 1D gas dynamics, though the images were not calibrated for quantitative purposes.

Generally, the development can be outlined as an initial compression of the gas/vapor within the multiphase interface ($t = 0.4[\mu s]$) followed by breakup of the parent droplets forming child droplets ($t = 0.4 - 8.4[\mu s]$), then growth of the child droplet cloud ($t = 8.4 - 98[\mu s]$), and lastly evaporation of the child droplets ($t = 98 - 253[\mu s]$). The image at $t = 0.4[\mu s]$ shows the breakup process and early cloud development as particles on the downstream side of the interface remain intact while those on the upstream side are already showing child droplet cloud growth. Droplet breakup initiates at different times depending on when the

shock wave intersects it, and occurs at different rates, dependent upon the parent droplet's size. As the shock traverses the droplet-gas curtain, the gas responds instantaneously, jumping to the post-shock conditions. At the same time, the droplets begin equilibrating with the gas through mass, energy, and momentum transfer. The momentum equilibration time is responsible for the droplets falling behind the gas interface, even before breakup occurs. Parent droplet deformation occurs before breakup, over a relatively short time, but could not be visualized as the droplet sizes under consideration were close to or under the diffraction limit of our optics.

Within the child droplet cloud, the smallest droplets equilibrate in speed with the post-shock gas near instantaneously. In contrast, the larger droplets lag behind and stretch the cloud (in the X direction), dropping further behind the gas/vapor interface. The cloud growth in the X direction can be attributed to the different equilibration times from the child droplet size distribution. The droplet cloud growth in the X-Y and X-Z directions can be attributed to the deformation rate of parent droplets, creating a radial velocity that transitions the child droplets outward. The growth in the X-Y and Y-Z planes is assumed to be symmetric for analysis purposes. Once growth ceases, it can be taken that the system has equilibrated in velocity.

Additionally, the intensity of scattered light from the droplets decreases significantly from the initial droplet clouds, near the initial breakup event, to the evolved and evaporating clouds at later times, as seen in figure 8. In this figure the sum of the image intensity is divided by the total area of droplet clouds, as identified by the algorithm discussed in section 4.2.Then, after finding the average intensity corresponding to a group of clouds at a specific time, all average cloud intensity values were normalized against the maximum average intensity of the complete data set. The initial increase in average intensity is due to the increased area for light scattering as single large parent droplets are converted into many small child droplets, as explained from Mie-theory Crowe, Sommerfeld, Tsuji et al. (1998). The initial sudden decrease in intensity can be explained by the stretching of the droplet clouds, as the cloud area increases greatly from the region before $\sim 10[\mu s]$ to that after. A slow decrease in average intensity occurs then as clouds are stretched, and the smaller child droplets begin to completely evaporate, marking a second decrease in intensity at about 150 $[\mu s]$.

Lastly, the particle survival time can be measured as the time when the intensity of scattered light for a droplet cloud drops to zero. The size of the parent droplet largely influences the evaporation time and the cloud conditions. The bigger the parent droplet, the larger the child droplets produced, leading to a longer survival time. From the experimental results, no droplet clouds were observed past $300[\mu s]$, while clouds were observed only intermittently from $250 - 300[\mu s]$, indicating that the evaporation time of the larger parent droplets (resulting child droplet clouds) should be in this range.

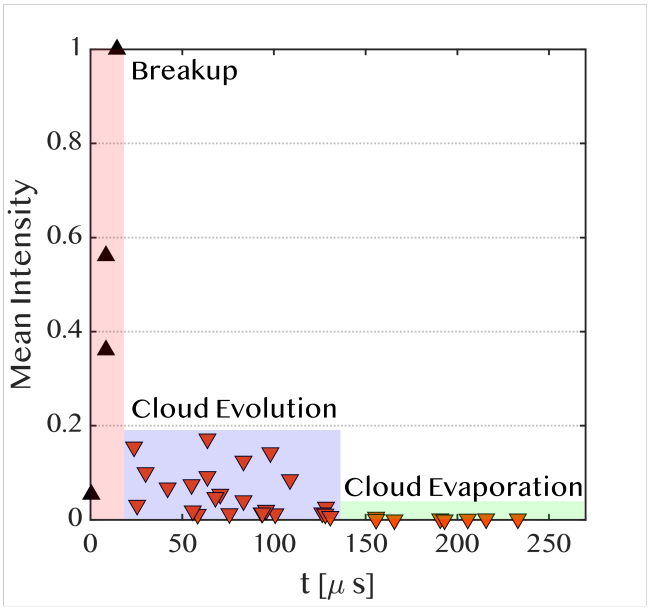

Figure 8: Average child droplet cloud intensity versus time, mean intensity is average maxi-mun cloud intensity

4.2. Particle Cloud Detection

The algorithm for child droplet cloud size detection consists of three main routines: image pre-processing and background correction, cloud boundary detection, and detected cloud acceptance/rejection. Once images are loaded, background subtraction is performed from the mean value of the background image before the shock. Image noise reduction is performed to improve the image restoration process, followed by an image median filter square of 5 [px] by 5 [px] to smooth droplet intensity within the cloud, and finally a 2-D Gaussian smoothing kernel filter to slightly blur the droplet cloud. A 2D gradient filter was then applied to the image to identify the cloud boundary quickly and reliably. The algorithm extracts from the detected droplet cloud boundary the length ΔX, width ΔY, mean intensity, and X distance traveled post-shock, and plots the results.

Figure 9: MATLAB algorithm for detecting cloud metrics

After the droplet clouds were detected, a mean of the cloud length and width were obtained for each image. Cloud length and widths beyond ± 1 standard deviation were rejected. These rejected cloud lengths were most often due to overlap with neighboring clouds. An example of the detected droplet cloud found with the algorithm can be seen in figure. 9. A subsequent routine in the algorithm calculates the upstream and downstream locations matching droplet cloud locations in frame B, with the initial parent droplet location from frame A. From the center of the detected cloud in frame B, we traced the pixel location of the most likely

parent droplet in frame A by matching the Y position. Lastly, the algorithm's detection is limited by the proximity of child droplets to one another in that droplets with spacing larger than the filter size will result in a discontinuous intensity contour. Thus, large trailing droplets may not be included in the cloud dimensions, producing a possible error on the order of 5 [%] for some clouds. On average, 15 ± 5 clouds are detected per experimental run, providing some statistical certainty and minimizing the effect of small random errors in our could dimensions.

4.3. Quantitative Description of Droplet Cloud Dynamics

Once the cloud boundary is detected in frame B, the droplet position is measured from the center of the interface in frame A to estimate the relative position (distance traveled) of the cloud head (downstream) and tail (upstream) over time, shown in figure. 9. Generally, more parent droplets were detected in frame A than child droplet clouds in frame B as time progressed. This is because the smallest parent droplets will change phase relatively quickly and are no longer detected in frame B, while the largest will persist much longer.

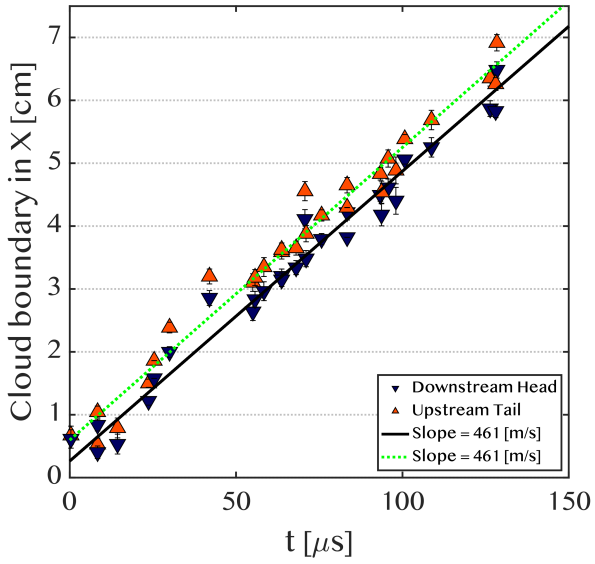

Figure 10: Cloud downstream and upstream positions versus time

As seen in figure. 10 at time 0 [μs], the parent droplets are immediately accelerated by the shock wave passage, breaking up and quickly equilibrating with the gas velocity ($\sim 461.3[m/s]$). It could be inferred that the smallest child droplets tend to accelerate faster and quickly reach equilibrium with the flow at the head (downstream edge) of the droplet cloud. Inversely, the largest child droplets within the distribution tend to fall behind, stretching out the droplet cloud and showing more significant cloud growth. Figures 11 and 12 display the average cloud length and width, shown as orange points, with error bars giving the bounds of lengths or widths of droplet clouds observed at that time. The cloud length and width increase in the first 70 [μs] and starts to plateau at late times as all child droplet sizes come to velocity equilibrium with the gas.

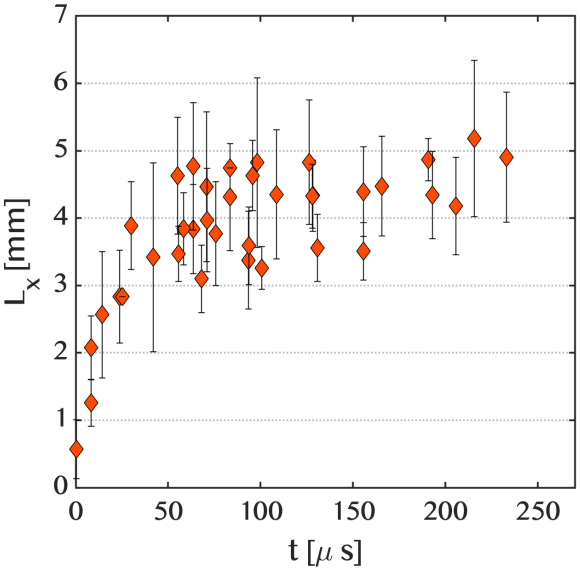

Figure 11: Cloud length L_x versus time

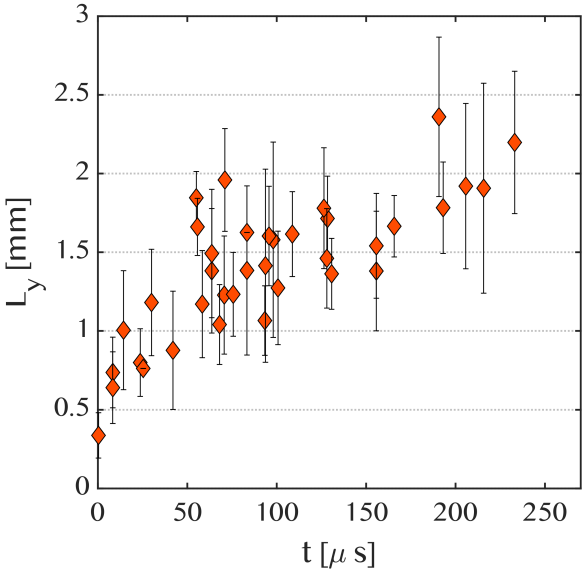

Figure 12: Cloud width L_y versus time

It must be emphasized that child droplet cloud growth is correlated with the parent droplet size distribution shown in section 3.2. The smallest parent droplets (below 6 [μm]) will have deformation, break up and phase change on similar time scales. However, as the parent droplet diameter increases, there is an increase in the breakup time and more considerably the evaporation time, leaving more time for child droplet cloud growth before complete evaporation. Observations of

the droplet clouds at $t > 300[\mu s]$ do not show discernible droplet clouds indicating that complete evaporation occurs at $300 > t > 250[\mu s]$.

5. Modeling of Experimental Results

In this section, a simplified model, the Child Droplet Cloud (CDC) model, is developed to explain the observed evaporation times and cloud growth. It was hypothesized in the previous sections that the child droplet cloud length resulted from a difference in equilibration times resulting from the child droplet size distribution. As such, this model predicts the trajectory of the parent droplet, and representative small and large child droplets to predict the cloud development in X and Y. Various breakup models, providing predicted breakup times and child droplet sizes, are tested to determine their fit to the experimental measurements. Further, the evaporation time is estimated based on the D^2 law modified to account for significant local vapor fractions when necessary. The use of these simplified models accounts for shock conditions, droplet breakup, and psychrometrics and allows the direct calculation of final child droplet cloud size and evaporation time without the need for numerical integration. The detailed equations of this model may be found in the appendix (8) while the following sections provide a mostly qualitative description of its functioning and its results.

5.1. Predicted Gas Properties

First, the gas conditions must be predicted based on the initial gas properties and shock strength. Two initial conditions were considered; one for the surrounding dry air and one for the acetone-vapor-saturated nitrogen within the multiphase interface. The post-shock conditions were solved using 1D gas dynamics. The surrounding air was calculated to have a post-shock pressure of $493.6[kPa]$, temperature of $516.6[K]$, and velocity of $461.3[m/s]$, at the mean shock Mach number of 2.09. For simplicity, the shock refraction problem is not solved at the gas interface (air and acetone-nitrogen mixture) since the interface is limited in size in the shock (Y-Z) plane ($\sim$ 50 [mm] interface width vs 140 [mm] tube width). Instead, the interface gas is assumed to achieve the same velocity as the post-shock air, and the transmitted shock strength predicted. Note this assumption will result in a mismatch in predicted pressure between the interface and surrounding gas, but eliminates the need for 2D gas dynamics simulations. With this assumption, the interface carrier gas is estimated to have a post-shock temperature of $461.1[K]$. The droplets are assumed to fall behind the interface carrier gas and into the surrounding dry air after initiation of the breakup process. It is then assumed that the child droplets and surrounding air reached the wet bulb temperature rapidly (see Duke-Walker et al. (2020); Paudel et al. (2018)). The wet bulb temperature was calculated based on psychrometric equilibrium conditions to be $T_{wb} = 328.3[K]$.

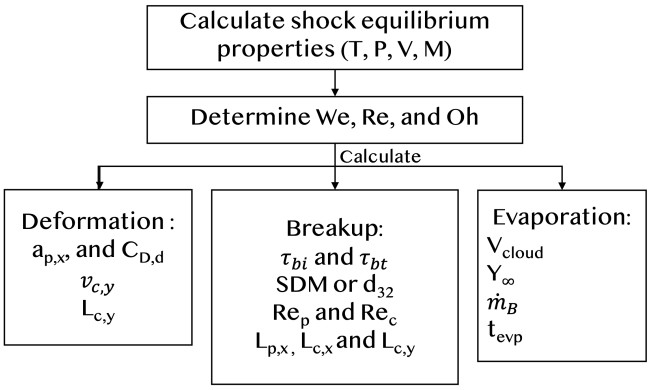

Figure 13: Modeling algorithm

5.2. Droplet Trajectories

The simple scenario of rigid spherical, non-deforming / breaking acetone droplet will be considered first to explain the effect of drag on droplet trajectories in the CDC model. The CDC model assumes that droplet-to-droplet interactions are negligible (interface droplet volume fractions were $< 1[\%]$) even within the child droplet cloud (droplet volume fractions quickly drop below $1[\%]$ during cloud evolution). Additionally, the droplet was assumed to begin accelerating when the incident shock has completely transited the droplet, and unsteady drag effects were not considered. A simple drag model was used (Eqns. 1), where the coefficient of drag was taken to follow the Klyachko (1934) drag model, shown in Eqn. 2. Cloutman (1988) provided an analytical solution for the droplet velocity (Eqn. 4 and 8) and position (Eqn. 5 and 9) over time (see Dahal and McFarland (2017) for more) for both $Re > 1000$ and $Re \leq 1000$ regimes. For our conditions, the acetone droplet will start on the high Re solution if it is larger than $\sim 8[\mu m]$ in diameter and then transition to the low Re solution as its velocity increases, Re decreases. Its final lag distance can then be estimated as the distance traveled relative to the gas once the droplet reaches 99 $[\%]$ of the gas velocity.

5.3. Deformation Model

Deformation effects are now added to the simple rigid droplet acceleration scenario as a necessary precondition for breakup. The effect of deformation is to increase both the drag coefficient and cross-sectional area of the droplet as it takes on an oblate form. Deformation was taken to occur as described by the TAB model O'Rourke and Amsden (1987) where the droplet's dynamics are considered as a forced mass-spring-damper system. The deformation process is taken to begin immediately when the shock wave completely transits the droplet and will end at the onset of breakup, if the breakup criteria are met.

The parent droplet will begin to oscillate from a sphere to a oblate-disk of equal volume, altering the drag forces experienced by the droplet. If the windward and leeward points are taken as the poles, then the diameter at the equator, d_a, will increase initially. The non-dimensional displacement of the equator is taken as $y^* = 2(d_a - d_p)/d_p$,

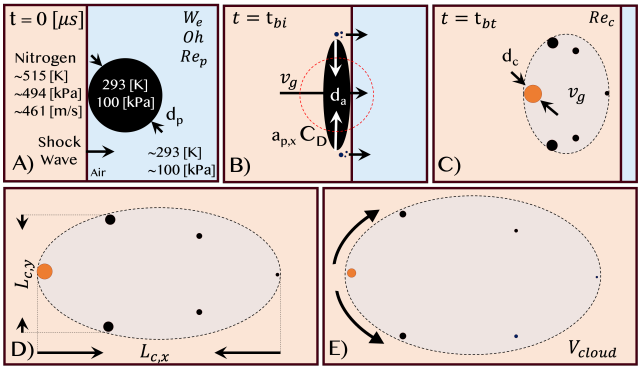

Figure 14: Schematic of the deformation and breakup process: A) Initial Parent droplet of diameter d_p, B) Maximum Deformation d_a, C) Representative Sauter mean child droplet diameter d_c, D) cloud development Trajectory, and E) Nearly evaporated particle

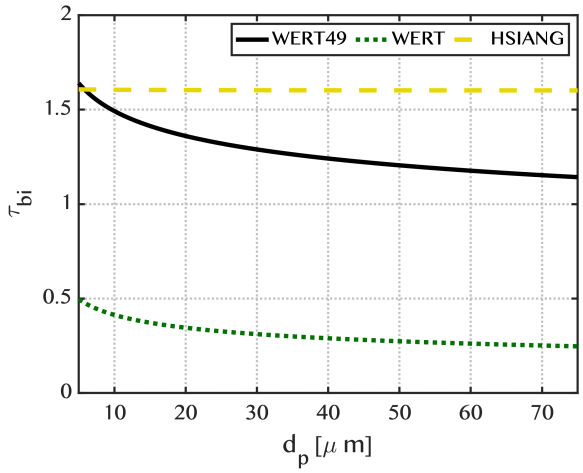

Figure 15: Breakup initiation versus parent diameter at Mach ~ 2.1 flow conditions

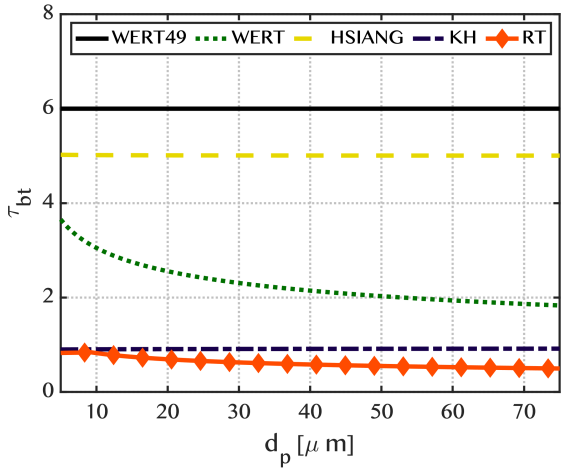

Figure 16: Breakup completion versus parent diameter at Mach ~ 2.1 flow conditions

where d_p is the initial diameter of the parent droplet. The equatorial diameter d_a will continue oscillating as y^* follows a decaying sine wave. If y^* exceeds a critical value of 1, meaning that the droplet has reached 150 [%] of its original equatorial diameter, then breakup will occur, ending the oscillation of the parent droplet.

Rather than track the parent droplet diameter as a function of time, its drag properties were derived from a weighting of the initial spherical and its fully deformed oblate spheroid shapes. Since it is known that the parent droplet will experience more time acting as a sphere than a disk Chou and Faeth (1998), when breakup is eminent, the drag properties are weighted to be $1/3$ of a sphere, and $2/3$ the final oblate spheroid. The drag acceleration term is weighted by the deformed area ratio (Eqn. 3) and modifies the drag coefficient (Eqn. 11), providing a closer representation of the drag forces experienced by the parent droplet before breakup. A representation of this process can be seen in figure. 14 B. At the onset of the breakup process, the child droplet outward radial velocity, $v_{c,y}$, is set based on the deformation rate from the TAB model Tanner (1997) as seen in Eqn. 16.

5.4. Breakup Models

Adding to the model for a deforming droplet, breakup is now considered. Many models exist for breakup, providing breakup times and child droplet sizes. A combination of theoretical, the KHRT model Beale and Reitz (1999), and empirical models such as those of Wert (1995), Duke-Walker et al. (2021), and Hsiang and Faeth (1992) have been implemented to predict the child droplet parameters. Since breakup parameters (e.g. We, Re, and Oh) for these models are set at the time of shock interaction, the properties of the post-shock acetone saturated interface gas are used. The breakup times for each of these models are based on the characteristic breakup time, t_c in Eqn 17, proposed by Nicholls and Ranger (1969). Breakup times can be nondimensionalized as $\tau_b = t/t_c$.

The KHRT model predicts that breakup occurs through two hydrodynamic instabilities on the droplet surface, the Kelvin-Helmholtz (KH) and Rayleigh-Taylor (RT) instabilities. For each instability the most unstable, fastest growing (Eqns. 19 and 21) wavelength is calculated (Eqns. 20 and 22). The child droplet sizes are taken to scale with this wavelength for each mechanism (Eqn. 24). The rate of production is taken as a function of the instability growth rate with parameters tuned to agree with the characteristic breakup time, t_c. The KH mechanism is taken to begin immediately after shock interaction, $\tau_i = 0$, and to precede deformation. The KH mechanism then continues at a sufficient rate to consume all droplet mass at the predicted final breakup time, $\tau_{bt,KH}$. The RT mechanism was taken to occur instantaneously at $\tau_{bt,RT}$ and may occur before the KH instability consumes the entirety of the parent droplet mass (figure. 16). The KH mechanism may be prevented when the most unstable wavelength becomes larger than the droplet

diameter. Sharma et al. (2022) suggests that $\lambda_{kh}/d_p < 0.1$, while Theofanous et al. (2012) suggests $\lambda_{kh}/d_p < 0.2$ and that RT instability cannot be dominant if this condition is met.

The empirical models are derived based on experimental observations of breakup driven by a shock interaction for droplet diameters on the order of 1 [mm]. For this work, the models of Wert (1995) (referred to as Wert model), Duke-Walker et al. (2021), a modification of Wert's model (referred to as Wert49 model), and Hsiang and Faeth (1992) (referred to as Hsiang model) have been tested against our experimental observations. These models predict that breakup will initiate at some time after shock interaction, t_{bi}, and end at t_{bt}, where these values are found as functions We and Oh (Eqns. 18 and 23). The functions used for each time may change with We, breakup regime. Since all cases presented are in the high Weber number regime, $W_e > 600$, there is only one applicable time correlation for each model. The breakup initiation time is constant at $\tau_{bi} \sim 1.6$ for Hsiang model, while it decreases with increasing We for both the Wert and Wert49 models taking on values of $\tau_{bi} \sim 0.35$ and $\tau_{bi} \sim 1.2$, respectively, in the We range of interest here (figure. 15). The total breakup time again takes on a constant value of $\tau_{bt} \sim 5$ for the Hsiang model, and a constant value of $\tau_{bt} = 6$ for the Wert 49 model, while for the Wert model the breakup time decreases with We approaching a value $\tau_{bt} \sim 2$ for the We numbers considered here. Figure 16 shows that the KH and RT mechanisms are much faster than the empirical models for the gas conditions considered here, though the Wert model approaches the KHRT times for large droplets $d_P > 70$.

The child droplet sizes produced are predicted as a function of the initial breakup parameters and times. While a range of sizes is produced during breakup, these models predict a single characteristic size for the child droplets, the Sauter mean diameter or d_{32} (Eqn. 24). This droplet size is predicted as ratio of the parent drop size, d_c/d_p. For each empirical model, the child droplet size ratio, d_c/d_p, asymptotes to a low value as We increases, $d_c/d_p \sim 0.1$ for the Wert49 and Hsiang models and $d_c/d_p \sim 0.05$ for the Wert model as seen on figure 17. A comparison of the child droplet sizes produced at our gas conditions is shown for each model in figure. 18. This figure shows that both Wert and RT models produced a similar particle diameter. Similarly, Wert49 and Hsiang are relatively close for small droplets, $d_p < 40[\mu m]$. Conversely, the KH child droplet sizes were an order of magnitude smaller than other models.

These small KH droplets will equilibrate with the surrounding gas nearly instantaneously due to their small size. Similar behavior has been observed in work related to the empirical models, and Chou and Faeth (1998) found that small droplets were observed at early times traveling near the gas velocity. The model proposed here, thus assumes that the smallest child droplet produced occurs at early time and is sufficiently small to equilibrate with the gas nearly instantaneously. For the KHRT model this droplet is produced at $\tau = 0$ and for the empirical models at $\tau = \tau_{bi}$.

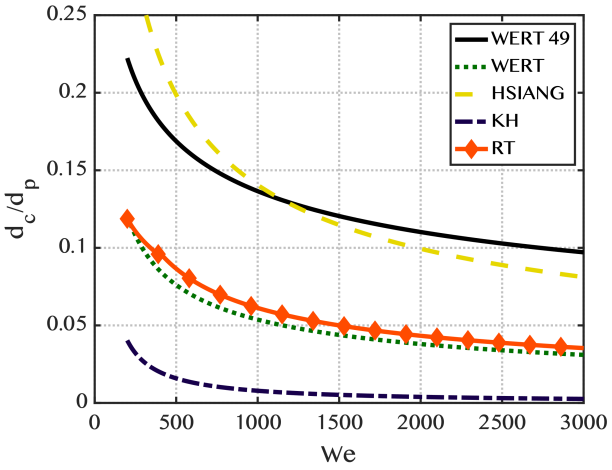

Figure 17: SMD ratio (d_c/d_p) vs We predicted by different breakup models

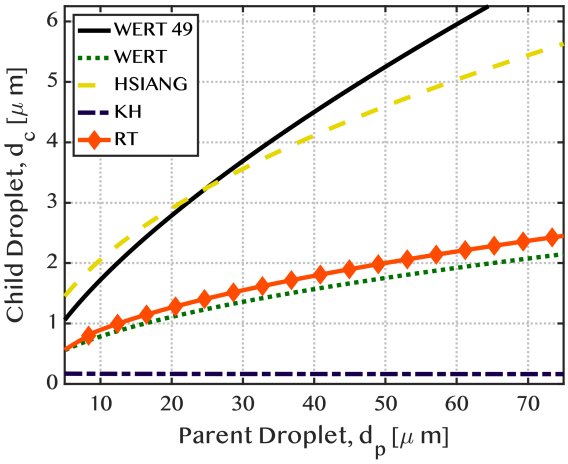

Figure 18: Parent vs Child droplet diameters predicted by different breakup models

Breakup ceases at $\tau = \tau_{bt}$, whether by onset of the RT mechanism or by completion of the KH or empirical breakup models. At this time, the child droplets produced are taken to have a diameter d_c (Eqn. 24, given by the empirical models, or RT mechanism (for our conditions RT breakup precedes KH completion).

With the child droplet production timing and sizes determined, the droplet trajectory model can be implemented to determine the path of two exemplar child droplets, the characteristic smallest and largest sizes (or KH and RT child droplets). The small droplet trajectory will track the downstream edge of the child droplet cloud, and for both the KH and empirical models the droplet is assumed to travel at the gas velocity from the moment of production. For the large droplets, the parent droplet trajectory must be tracked until $\tau = \tau_{bt}$ as in section 5.3. This provides its velocity and lag distance from τ_{bi}, when the small child droplet is produced and begins traveling with the gas, to τ_{bt}, when the

large droplet is produced and takes on its own trajectory. The child droplet trajectory starts at the parent droplet's position and velocity, including the radial velocity predicted by the deformation model. It is tracked using the equations presented in section 5.2 for both the x and y components of velocity. The final cloud dimensions may be estimated when $v_{c,x} = 0.99 v_{g,x}$, which allows an estimate of the maximum volume of the individual cloud to predict its evaporation time.

5.5. Evaporation Models

Up to this point, droplet deformation and breakup have been considered to be independent of phase change. We now add evaporation to the deforming and breaking droplet case to determine when the resulting child droplets should completely evaporate. A simple estimation of evaporation rates can be provided from the D^2 law Crowe et al. (1998) and the instantaneous droplet vaporization rate provided by the Spalding model, $\dot{m}_B$ (Eqn. 31), Abramzon and Sirignano (1989). The evaporation rate of the parent droplet is considered to be negligible and the D^2 lifetime of the largest child droplet, after formation at τ_{bt}, is taken to predict when the child droplet cloud should no longer be visible in experimental Mie-scattering images.

The effect of cloud gas saturation by vapor is considered when significant. The cloud total volume V_{cloud} is calculated as the volume of an ellipsoid, where the child droplet maximum radial displacement $L_{c,y}$ is used for the Y and Z dimensions and the cloud trajectory parallel to the shock wave $L_{c,x}$ is used for the X dimension. The maximum vapor mass fraction achievable in the child droplet cloud, Y_{max}, is predicted using the cloud volume, parent droplet mass, and thermodynamic functions. This value was found to be negligible, $< 1\%$, for the Wert49 and Hsiang breakup models, but in excess of the saturation mass fraction for the Wert and KHRT models at the parent droplet sizes considered. Thus, complete evaporation of the child droplet cloud would not be predicted to occur for the KHRT and Wert model, as seen in figure. 19, though mixing and diffusion effects not included in the CDC model would result in complete evaporation at much greater times.

To calculate the droplet vaporization rate of the child droplet $\dot{m}_B = f(\mathcal{D}_v@T_f, d_c, \rho_f, Sh, B_M)$, child droplets were considered to lag into the surrounding dry gas at the post-shock conditions (as observed in our experimental measurements). Since velocity equilibrium is achieved at early times relative to the complete evaporation time, we take that evaporation occurs primarily in the free convection regime, setting the Sherwood number to 2. The Spalding mass transfer number, B_M (Eqn. 27), is calculated assuming that the vapor mass fraction in the cloud gas is at its maximum value, $Y_\infty = Y_{max}$. This assumption works well as this value is exceeding low ($< 1[\%]$) for the Wert49 and Hsiang models, meaning that it has little effect even though its variation with time is not observed. For the Wert and KHRT models, saturation is achieved and the variation of Y_∞ with time will not alter the outcome, that complete evaporation will not occur. A time-varying model for the vapor fraction can be implemented using the approach outlined here but was unnecessary at this time. The surface vapor fraction, Y_S, is found by assuming that the surface layer of gas is at the droplet temperature and is saturated with vapor.

Mass transport properties (e.g. Sh and $\mathcal{D}_v$) were evaluated at the film temperature T_f and density ρ_f. The film properties are estimated as being 1/3 the free stream value (post shock dry gas conditions) and 2/3 the surface values, e.g. film weighting factor $A_r = 1/3$ in Eqn. 28) Abramzon and Sirignano (1989). The temperature at the surface of the droplet was taken to be the uniform droplet temperature set to the wet bulb value $T_p = T_{wb}$. The surface gas density was evaluated for the saturated mix of gas and vapor at Y_S and T_S. A total evaporation time was computed using the initial steady-state mass transfer rate, $\dot{m}_B$, to find the time rate of change of the diameter squared, $\frac{d}{dt}\left(d_c^2\right)$. The D^2 law assumes that this value is constant over the life of the droplet, thus we can predict the total evaporation time by predicting when $d_c^2 = 0$ (see Eqns. 32 and 33).

5.6. Comparison of Models to Experimental Data

The results of the CDC model are plotted for each model for two parent droplet sizes, $d_{10} \sim 14.16[\mu m]$ and $d_{32} \sim 37.3[\mu m]$, in figure 19. The performance of the CDC model is strongly dependent on droplet acceleration during deformation, the breakup time, and child droplet size. The droplet trajectory was modified, as the deforming parent droplet is accelerated and child droplets are produced. The parent droplet will experience its highest acceleration as the shape deforms to an oblate disk, resulting in a shorter velocity equilibration time. This effect modifies the parent droplet trajectory and child droplet cloud length at early times, from τ_{bi} to τ_{bt}, and may be observed clearly in the Wert49 and Hsiang droplet model results. Even though the Wert49 and Hsiang models create similar child droplet sizes for a 37.3 $[\mu m]$ parent droplet, the Hsiang model breakup times, being shorter, reduce the parent droplet lag and thus the child droplet cloud length. Further, the larger the parent droplet, the greater the parent droplet lag distance, despite the lower acceleration rate.

The KHRT model considers the droplet to immediately break up, producing small child droplets that equilibrate rapidly with the shocked gas. Since the KH time is longer than the RT time, the droplet will be stripped of mass by the KH initially; however, RT breakup will terminate the breakup process. The RT mechanism produces slightly larger child droplets, but still possesses short equilibration times. The parent droplet lag, over the short time between KH onset and RT final breakup, contributes significantly to the cloud length. The Wert model, having only slightly larger breakup times and similar child droplet sizes, produces slightly large cloud lengths (figure. 19). Both the KHRT and Wert models have cloud volumes that are sufficiently small that the cloud gas will be saturated, thus evaporation will not consume all the liquid droplet mass unless additional cloud mixing effects are included. This evaporation effect is,

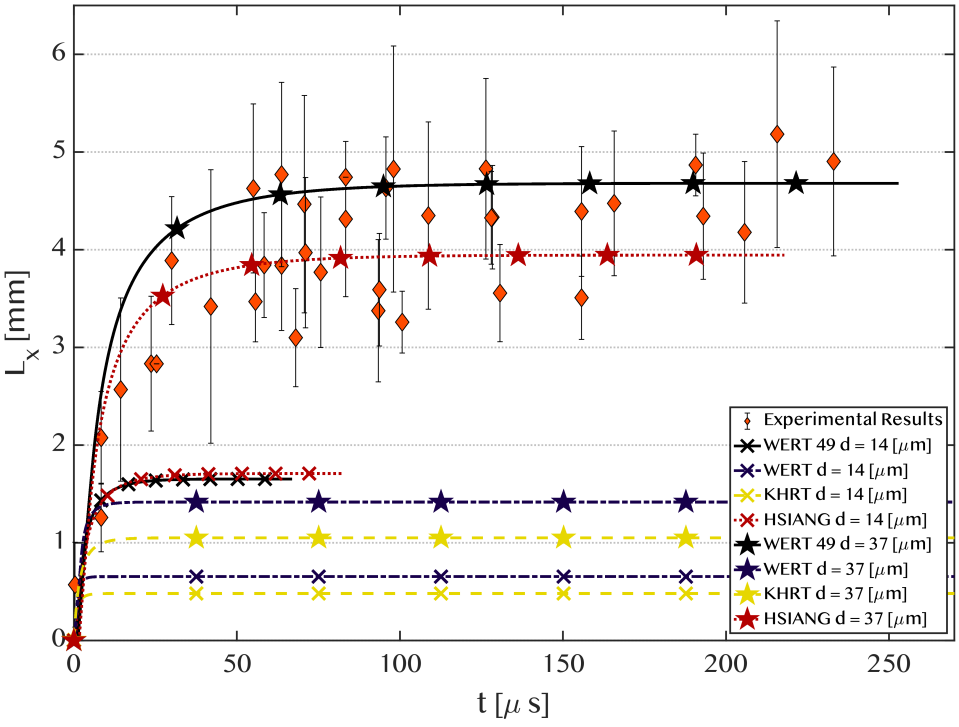

Figure 19: Cloud length L_x versus time comparison between model and experimental results

in essence, a particle-particle effect, sometimes referred to as three-way coupling and typically limited to high volume fractions.

The Wert49 and Hsiang models produce longer breakup times and larger child droplet sizes, resulting in larger child droplet clouds. As discussed in the previous section, vapor fractions were much smaller as the cloud volume increased with cloud length and by the square of the cloud width. Thus, the child droplets evaporate as if they are in the free stream gas, without affecting one another, with no particle-particle effects. Predictions from the Wert49 and Hsiang models show better agreement when compared with the experimental measurements in terms of the child droplet cloud size, the transient acceleration response during deformation, and the predicted evaporation times. The varying evaporation times between the d_{32} and d_{10} droplet sizes help to explain the slight upward trend in cloud length at late times. As clouds from small parent droplets evaporate, the mean cloud size trends towards the larger clouds produced by larger parent droplets.

Overall, the Wert49 model produced the best match to the experimental data, though it still under predicts the largest cloud lengths. One reason for this may be that child droplet sizes are certainly produced in excess of the d_{32} size as it is only a statistical representation of the size distribution tail. The trajectory of the small parent droplet cloud sizes predicted is also somewhat smaller than experimental measurements. One possible reason is that the parent droplet experiences a stronger drag than our model predicts; recall that the current model uses an average of drag properties estimated for a deforming parent droplet.

With this in mind, the data of Kobiera et al. (2009) was considered for further validation of the proposed CDC model. These experiments measured the child droplet cloud lengths over time for various millimeter-sized ($0.6 - 2.0$ [mm]) n-hexane droplets. Owing to their larger size, these droplets will have longer evaporation times relative to their velocity equilibration times. This data serves then to test the CDC model on larger parent droplets, in a different We regime with little evaporation effects. Both the Wert49 and Hsiang breakup mechanisms showed some agreement, while the KHRT and original Wert model had poor agreement, and thus, are not shown. Figure 20, shows the data of Kobiera et al. (2009), reproduced by digitization of figures 15 and 18 in the cited paper.

Overall, agreement is good for the Wert49 model at late times for the 1-2 [mm] droplets (within ~ 9[%] error). The early time trajectories of the droplets show less agreement as the experimental data for the 0.6-1.3 [mm] droplets show an inflection that cannot be reproduced by the CDC model, and is not consistent with the 2 [mm] droplet data. The 1 and 1.3 [mm] experimental data also show a sudden decrease in cloud length at $t \sim 300[\mu s]$ that cannot be explained by the physics considered in this paper. The 0.6 [mm] droplet data aligns closely with the 1 [mm] data and thus does not agree well with the Wert49 CDC model predictions. The Hsiang model matched the results well for the 1.3 [mm] size, due in part to the anomalous drop at $t \sim 300[\mu s]$, but the

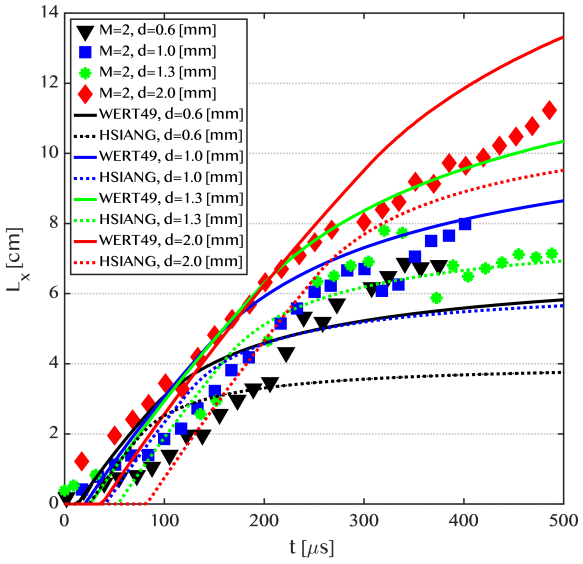

Figure 20: Cloud length L_x results: utilizing the empirical Wert49 and Hsiang breakup model

Wert 49 model showed overall better agreement. Without further information on the experimental conditions of this work, we cannot provide further insight as to the sources of disagreement. Other breakup models showed poorer agreement, with the Wert and KHRT models having greater than $\sim$ 80[%] error. The Wert49 model fit can be improved by increasing the parent droplet acceleration considering a higher weighting of the oblate versus sphere properties over the breakup time (see section 8.4, a weighting of 1/2 worked well).

6. Conclusion

Experiments were performed to examine the shock-driven simultaneous breakup and evaporation of small droplets. The droplet sizes ($14.16 < d_p < 37.3[\mu m]$) and shock wave Mach number ($M \sim 2.09$) produced Weber numbers in the range of $600 < We < 1800$ and Reynolds numbers in the range of $1600 < Re < 4400$, resulting in rapid velocity equilibration times and droplet evaporation. A simple model, the child droplet cloud (CDC) model, was developed to provide further insight into the experimental data and the physics of small droplet breakup and evaporation. Four breakup models were considered, one analytical model (KHRT model) and three empirical models (Wert, Hsiang, and Wert49) based on experimental observations of larger droplets at lower shock wave Mach numbers. Evaporation times were estimated using the D^2 law for characteristic large child droplets, accounting for the saturation of the cloud gas. Child droplet cloud lengths and evaporation times were estimated for both the d_{10} and d_{32} sizes measured in experiments.

The empirical models considered provided the best prediction of the child droplet cloud length and evaporation time. The Wert49 model, a modified version of the Wert model Wert (1995) developed in our previous work Duke-Walker et al. (2021), was found to most closely predicted child droplet trajectories and evaporation time. The model deficiencies are likely due to the underprediction of the parent droplet drag force during breakup or possibly due to the presence of larger child droplets than predicted. The Hsiang breakup model Hsiang and Faeth (1992) produced similar results but predicted slightly smaller droplet cloud lengths than measured. The CDC model, with the Wert49 breakup mechanism, also compared well to previously published data for millimeter-sized droplets accelerated by a $M = 2$ shock wave ($21,000 < We < 70,000$) Kobiera et al. (2009). Both models found that child droplet clouds were large enough that the vapor content remained low and droplet evaporation was not effected by neighboring child droplets.

The KHRT model predicted rapid production of very small KH child droplets followed by an RT breakup event terminating the breakup process. The RT droplet sizes predicted were larger than the KH droplets and similar in size to the droplet sizes predicted by the original Wert model. While the Wert and KHRT models produced similar child droplet sizes, the Wert model predicted larger cloud lengths due to its greater breakup times and resulting increase in parent droplet lag distance. Both models produced sufficiently small cloud volumes that vapor saturation was achieved, thus evaporation could not completely consume the liquid mass. The KHRT model resulted in the smallest child cloud lengths.

The CDC model results indicate that cloud lengths are largely driven by overall breakup times, parent droplet drag forces during breakup, and child droplet size distributions, resulting in varying lag distances. Overall, the empirical models derived from experiments at low We produce better agreement with our observations at high We. An explanation for this might be found in the KHRT model, as it predicts breakup as a function of surface hydrodynamic instabilities, rather than a function of We. For our case, the KHRT model predicted that RT growth rates would be significant, preempting the KH breakup process, due to the rapid acceleration of small droplets at high velocity. The KHRT model also predicts RT breakup for large droplets at low We, similar to the experimental conditions used for the empirical model. Further, the KHRT model predicts the early formation of very small droplets, as assumed by the CDC model. Thus, the underlying interpretation of the breakup process in the KHRT model has merit. Further analysis of the KH and RT mechanisms should be undertaken to provide better timing for the onset of the RT mechanism and better representative child droplet sizes. For now, the CDC model with the Wert49 breakup model provides the best match for child droplet cloud sizes and evaporation times for parent drops in the range of $700 < We < 70,000$ and $Oh < 0.1$.

Our future experimental work will focus on understanding the behavior of the acceleration term and breakup times

on an interface composed of monodisperse droplets, in order to better determine the effects of droplet diameter on breakup and evaporation. Future theoretical work should focus on deriving more accurate parameters for the KH and RT instabilities on a breaking droplet. The CDC model will be implemented in our particle-in-cell simulations with more advanced time-varying deformation, drag, and evaporation models. Experimental observations of surface instabilities are needed for small droplets at high velocities. High-resolution simulations may also yield much needed insight into the interface physics.

7. Acknowledgements

This work was supported by the National Science Foundation through award number 2053154 and the Office of Naval Research through contract number N00014-20-1-2796.

References

Abramzon, B., Sirignano, W.A., 1989. Droplet vaporization model for spray combustion calculations. International journal of heat and mass transfer 32, 1605–1618.

Balakumar, B., Orlicz, G., Tomkins, C., Prestridge, K., 2008. Simultaneous particle-image velocimetry–planar laser-induced fluorescence measurements of richtmyer–meshkov instability growth in a gas curtain with and without reshock. Physics of Fluids 20, 124103.

Beale, J.C., Reitz, R.D., 1999. Modeling spray atomization with the kelvin-helmholtz/rayleigh-taylor hybrid model. Atomization and sprays 9.

Black, W.J., Denissen, N.A., McFarland, J.A., 2017. Evaporation Effects in Shock-Driven Multiphase Instabilities. Journal of Fluids Engineering 139. URL: https://doi.org/10.1115/1.4036162, doi:10.1115/1.4036162. 071204.

Chou, W.H., Faeth, G., 1998. Temporal properties of secondary drop breakup in the bag breakup regime. International journal of multiphase flow 24, 889–912.

Cloutman, L.D., 1988. Analytical solutions for the trajectories and thermal histories of unforced particulates. American Journal of Physics 56, 643–645.

Crowe, C., Sommerfeld, M., Tsuji, Y., et al., 1998. Multiphase Flows with. CRC Press.

Dahal, J., McFarland, J.A., 2017. A numerical method for shock driven multiphase flow with evaporating particles. Journal of Computational Physics 344, 210–233. URL: https://linkinghub.elsevier.com/retrieve/pii/S0021999117303625, doi:10.1016/j.jcp.2017.04.074.

Duke-Walker, V., Allen, R., Maxon, W.C., McFarland, J.A., 2020. A method for measuring droplet evaporation in a shock-driven multiphase instability. International Journal of Multiphase Flow 133, 103464.

Duke-Walker, V., Maxon, W.C., Almuhna, S.R., McFarland, J.A., 2021. Evaporation and breakup effects in the shock-driven multiphase instability. Journal of Fluid Mechanics 908.

Goossens, H., Cleijne, J., Smolders, H., Van Dongen, M., 1988. Shock wave induced evaporation of water droplets in a gas-droplet mixture. Experiments in fluids 6, 561–568.

Guildenbecher, D.R., Gao, J., Chen, J., Sojka, P.E., 2017. Characterization of drop aerodynamic fragmentation in the bag and sheet-thinning regimes by crossed-beam, two-view, digital in-line holography. International journal of multiphase flow 94, 107–122.

Hsiang, L.P., Faeth, G., 1992. Near-limit drop deformation and secondary breakup. International Journal of Multiphase Flow 18, 635–652. URL: https://linkinghub.elsevier.com/retrieve/pii/030193229290036G, doi:10.1016/0301-9322(92)90036-G.

Kirar, P.K., Soni, S.K., Kolhe, P.S., Sahu, K.C., 2022. An experimental investigation of droplet morphology in swirl flow. Journal of Fluid Mechanics 938.

Klyachko, L., 1934. Heating and ventilation. USSR Journal Otopl. i Ventil .

Kobiera, A., Szymczyk, J., Wolański, P., Kuhl, A., 2009. Study of the shock-induced acceleration of hexane droplets. Shock Waves 18, 475–485.

Lang, R.J., 1962. Ultrasonic atomization of liquids. The journal of the acoustical society of America 34, 6–8.

Leiby, M., 2021. Ultrasonic spray nozzles. URL: https://microspray.com/nozzles/.

Liu, A.B., Mather, D., Reitz, R.D., 1993. Modeling the effects of drop drag and breakup on fuel sprays. SAE Transactions , 83–95.

Loomis, D.J.S., . Produce orthonormal view from oblique projective image. URL: https://johnloomis.org/ece564/notes/tform/planar/html/planar2.html.

Mauro, S., Brusca, S., Lanzafame, R., Famoso, F., Galvagno, A., Messina, M., 2017. Small-scale open-circuit wind tunnel: Design criteria, construction and calibration. International Journal of Applied Engineering Research 12, 13649–13662.

Meng, J., Colonius, T., 2018. Numerical simulation of the aerobreakup of a water droplet. Journal of Fluid Mechanics 835, 1108–1135. doi:10.1017/jfm.2017.804.

Middlebrooks, J.B., et al., 2019. Shock tube experimentation utilizing advance diagnostics for the study of an impulsively accelerated multiphase cylinder. Ph.D. thesis. University of Missouri–Columbia.

Nicholls, J., Ranger, A., 1969. Aerodynamic shattering of liquid drops. AIAA Journal 7, 285–290.

Orlicz, G.C., 2007. Shock driven instabilities in a varicose, heavy-gas curtain: Mach number effects. Ph.D. thesis. University of New Mexico.

O'Rourke, P.J., Amsden, A.A., 1987. The TAB method for numerical calculation of spray droplet breakup. Technical Report. Los Alamos National Lab.(LANL), Los Alamos, NM (United States).

Park, G., Yeom, G.S., Hong, Y.K., Moon, K.H., 2017. Experimental study of time-dependent evolution of water droplet breakup in high-speed air flows. International Journal of Aeronautical and Space Sciences 18, 38–47.

Paudel, M., Dahal, J., McFarland, J., 2018. Particle evaporation and hydrodynamics in a shock driven multiphase instability. International Journal of Multiphase Flow 101, 137–151. URL: https://www.sciencedirect.com/science/article/pii/S0301932217306523, doi:https://doi.org/10.1016/j.ijmultiphaseflow.2018.01.008.

Pilch, M., Erdman, C.A., 1987. Use of breakup time data and velocity history data to predict the maximum size of stable fragments for acceleration-induced breakup of a liquid drop. International journal of multiphase flow 13, 741–757.

Sharma, S., Chandra, N.K., Basu, S., Kumar, A., 2022. Advances in droplet aerobreakup. The European Physical Journal Special Topics , 1–15.

Stefanitsis, D., Koukouvinis, P., Nikolopoulos, N., Gavaises, M., 2021. Numerical investigation of the aerodynamic droplet breakup at mach numbers greater than 1. Journal of Energy Engineering 147, 04020077. URL: https://ascelibrary.org/doi/abs/10.1061/%28ASCE%29EY.1943-7897.0000720, doi:10.1061/(ASCE)EY.1943-7897.0000720, arXiv:https://ascelibrary.org/doi/pdf/10.1061/%28ASCE%29EY.1943-7897.0000720.

Stefanitsis, D., Strotos, G., Nikolopoulos, N., Kakaras, E., Gavaises, M., 2019. Improved droplet breakup models for spray applications. International Journal of Heat and Fluid Flow 76, 274–286. URL: https://www.sciencedirect.com/science/article/pii/S0142727X18309007, doi:https://doi.org/10.1016/j.ijheatfluidflow.2019.02.010.

Tanner, F.X., 1997. Liquid jet atomization and droplet breakup modeling of non-evaporating diesel fuel sprays. SAE transactions , 127–140.

Theofanous, T., Mitkin, V., Ng, C., Chang, C., Deng, X., Sushchikh, S., 2012. The physics of aerobreakup. ii. viscous liquids. Physics of Fluids 24, 022104.

TSI, . Phase doppler particle analyzer manual. URL: https://tsi.com/products/fluid-mechanics-systems/phase-doppler-particle-analyzer-(pdpa)-systems/.

Wert, K., 1995. A rationally-based correlation of mean fragment size for drop secondary breakup. International Journal of Multiphase Flow 21, 1063–1071.

Widdecke, N., Klenk, W., Frohn, A., 1995. Impact of strong shock waves on monodisperse isopropanol droplet streams, in: Shock Waves@ Marseille III. Springer, pp. 89–94.

8. Child Droplet Cloud Model Details

8.1. Predicted Gas Properties

Post-shock properties (pressure, temperature, and velocity) were calculated using the ideal gas shock-jump equations. Phase change properties (e.g. saturation pressure and latent heat) and transport properties (e.g. viscosity) were taken from Engineering Equation Solver (EES). Gas mixture properties were calculated assuming ideal gas mixtures and psychrometric equilibrium. EES iteratively solved the system of equations of the CDC model using a forward Euler time marching method (1^{st} order accuracy in space and time).

8.2. Drag model

The simple drag force for a spherical rigid particle is calculated as $F_D = a_p m_p$, where m_p is the mass of the particle and a_p is the particle acceleration shown in Eqn. 1, where v_p is the particle velocity, $C_{D,s}$ is the drag coefficient of a sphere, and ρ_g and ρ_p the gas and particle densities.

$$a_p = C_{D,s}\frac{3}{4}\frac{\rho_g}{\rho_p}\frac{|v_g - v_p|}{d_p}\left(v_g - v_p\right) \tag{1}$$

The drag coefficient for a simple spherical droplet is taken to follow the Kliatchko drag model Klyachko (1934), shown in Eqn. 2, where μ_g is the gas kinematic viscosity.

$$C_{D,s} = \begin{cases} 24/Re + 4/Re^{1/3} & Re \le 1000 \\ 0.424 & Re > 1000 \end{cases} \tag{2}$$

8.3. Droplet Trajectories

Analytical solutions to Eqn. 1 with $C_{D,s}$ from Eqn. 2 were presented by Cloutman (1988) and used to model the particle dynamics. The cloud length is imagined as the distance between a small child droplet created at $t = t_{b,i}$ traveling at the gas velocity and the location of a characteristic large child droplet created at $t = t_{bt}$. It is tracked as a function of the lag distance of the largest child droplet from the moment the first small droplet is created, $t = t_{bi}$. The lag distance is defined as the distance between a particle and the gas it was initialized in, $L_x(t) = |v_{g,j}t - x_{p,j}(t)|$ where j is the index x or y, $v_{g,j}$ is the gas velocity component and $x_{p,j}(t)$ is the instantaneous coordinate of a particle with $x_{p,j}(t=0) = 0$.

The total lag distance of the large child droplet is found as the sum of the parent droplet lag distance from $t = t_{bi}$ to $t = t_{bt}$ and the large child droplet thereafter, $t > t_{bt}$. This distance is taken to be the cloud length, $L_j(t) = L_{p,j}(t_{bt}) + L_{c,j}(t)$. The process for calculating the individual lag distances is outlined in the steps below. It is assumed that the shock acceleration occurs only in the x direction.

(1) The drag acceleration coefficient of the parent droplet, $A_{p,x}$, is calculated assuming constant drag properties produced by a weighted average of a sphere and an oblate disk (see section 5.3). The weighted properties are assigned a subscript of d. Since all parent droplets had $Re > 1000$, the velocity and trajectory were computed following the high-speed solution (Eqn. 3).

$$A_{p,x} = \frac{3}{4}C_{D,d}\frac{\rho_g}{\rho_p}\left[\frac{{d_p}_d{}^2}{d_p^3}\right] \tag{3}$$

(2) The parent droplet velocity, $v_{p,x}(t)$, is calculated as

$$v_{p,x}(t) = v_{g,x}/\left[1 + A_{p,x}v_{g,x}t\right] \quad \text{if } t \le t_{bt} \tag{4}$$

(3) The parent droplet lag distance, $L_{p,x}$ is calculated from breakup initiation to completion, $t_{bi} \le t \le t_{bt}$, starting with a position $x_{p,x}(t_{bi}) = 0$. Since the shock acceleration is only in the x direction, $L_{p,y} = 0$ and $v_{g,y} = 0$.

$$\begin{aligned} &L_{p,x}(t) = x_{p,x}(t_{bi}) + A_{p,x}^{-1} ln[1 + A_{p,x}v_{g,x}(t - t_{b,i})] \\ &\text{if } t_{bi} \le t \le t_{bt} \end{aligned} \tag{5}$$

(4) A large child droplet is produced at $t = t_{bt}$ with initial x velocity of the parent droplet, $v_{c,j}(t_{bt}) = v_{p,j}(t_{bt})$ and y velocity given by the TAB model (see section 8.4. The velocity of the child droplets is small enough, low $Re < 1000$, such that they follow the low-speed solution from Cloutman (1988) with constants B_c, and C_c presented in eqns. 6 and 7, where d_c is the large child droplet diameter. The velocity is then calculated as shown in Eqn. 8.

$$B_c = 4.5\left[\frac{4\mu_g}{{d_c}^2\rho_p}\right] \tag{6}$$

$$C_c = \frac{3^{-1}}{2^{1/3}}\left[\frac{d_c\rho_g}{2\mu_g}\right]^{2/3} \tag{7}$$

$$\begin{aligned} &v_{c,j}(t) = \left[\left(v_{c,j}(t_{bt})^{-\frac{2}{3}} + C_c\right)e^{\frac{2B_c(t-t_{bt})}{3}} - C_c\right]^{-1.5} \\ &\text{if } t > t_{bt} \end{aligned} \tag{8}$$

(5) The lag distance of the large child droplet is defined with respect to its origin as $L_{c,j}(t_{bt}) = 0$. The child drop lag distance is shown in Eqn. 9.

$$\begin{aligned} L_{c,j}(t) = \; &\frac{3}{B_cC_c}\Big| \; v_{c,j}(t_{bt})^{1/3} - v_{c,j}(t)^{1/3} + \\ &C_c^{-1/2}tan^{-1}\left({C_c}^{-1/2}v_{c,j}(t_{bt})^{-1/3}\right) - \\ &C_c^{-1/2}tan^{-1}\left({C_c}^{-1/2}v_{c,j}(t)^{-1/3}\right) \Big| \\ &\text{if } t > t_{bt} \end{aligned} \tag{9}$$

(6) The total child droplet cloud length and width can now be calculated as a function of t. The maximum cloud size is calculated when velocity equilibrium is achieved, $v_{c,i} = 0.01 v_{g,i}$. By substituting these values into Eqn. 9, and adding the total parent drop lag distance, the maximum cloud dimension are obtained. It is assumed that the z cloud dimension is the same as the y dimension.

(7) Droplet trajectory were calculated until $t = t_{evp}$, as show in section 8.6.

8.4. Deformation Model

The parent droplet drag properties were calculated by taking a weighted average between a sphere and an oblate disk properties. This approach follows the results of Chou and Faeth (1998). The average deformation drag coefficient $C_{D,d}$ and an effective particle deformed diameter d_{p_d} were calculated below where the maximum distortion d_a was taken when $y^* = 2(d_a - d_p)/d_p = 1$.

$$d_{p_d} = \sqrt{{d_p}^2 \cdot (1 - y^*) + {d_a}^2 \cdot y^*} \tag{10}$$

$$C_{D,d} = C_{D,s} \cdot (2/3) + C_{D,dsk} \cdot (1/3) \tag{11}$$

The parent droplet deformation rate was computed using the TAB model O'Rourke and Amsden (1987) to provide a predicted initial child droplet radial velocity. It should be noted that the TAB model deformation rate would also indicate the breakup initiation time, t_{bi}, but this time is supplanted by the prescribed breakup models for cloud length predictions. While these t_{bi} values are similar, this does create a small inconsistency in this approach. Nevertheless, the TAB model was used to provide an estimate for the child droplet radial velocities as outlined below.

(1) The oscillation frequency for droplet oscillations, ω is calculated using Eqn. 12 where $C_k = 8$, $C_b = 0.5$ and $C_F = 1/3$ are the fundamental oscillation frequency, north and south amplitude of oscillation described by O'Rourke and Amsden (1987). This equation assumes that the viscosity of the liquid has a negligible effect on the oscillation frequency as is true for our case (acetone).

$$\omega = \left[\frac{C_k \sigma}{\rho_p (d_p/2)^3} \right]^{1/2} \tag{12}$$

(2) The surface velocity of the droplet is calculated from the deformation rate.

$$\dot{y}(t) = W_e \left[\frac{C_F}{C_k C_b} \right] \cdot \omega \cdot sin(\omega \cdot t) \tag{13}$$

(3) The surface velocity is assumed to reach a maximum at the time of maximum distortion, t_d.

$$t_d = cos^{-1} \left(1 - \frac{12}{W_e} \right) / \omega \tag{14}$$

(4) The child droplet velocity does take on the full value of the surface velocity but is instead reduced by a surface energy balance factor, α, as explained by Tanner (1997).

$$\alpha^2 = \frac{5}{4} C_{D,s} + \frac{18}{We} (1 - d_p/d_c) \tag{15}$$

$$v_{c,y}(t_{bt}) = \alpha \dot{y}(t_d) \tag{16}$$

8.5. Breakup Models

The breakup times and child droplet sizes are set by one of the four models discussed in the main text (KHRT, Wert, Hsiang, and Wert49) as follows:

(1) The breakup parameters (We, Re, and Oh) are calculated for the post-shock interface gas condition as described in the main text. The characteristic breakup time t_c is calculated in Eqn 17.

$$t_c = \frac{d}{v_g} \left(\frac{\rho_p}{\rho_g} \right)^{0.5} \tag{17}$$

(2) The breakup initiation times, $t_{bi,t} = \tau_{bi,t} \cdot t_c$, are calculated from the non-dimensional breakup times as given in Eqn. 18, where $We_\delta = (We - 12)$. The KH initiation time is by definition 0.

$$\tau_{bi} = \begin{cases} 1.9 We_\delta^{-0.25} & \text{Wert} \\ min(3, 3.3284 We_\delta^{-0.131}) & \text{Wert49} \\ \frac{1.6}{1-(Oh/7)} & \text{Hsiang} \\ 0 & \text{KH} \end{cases} \tag{18}$$

(3) For the KHRT model, the growth rate (Eqns. 19 and 21) and wavelength (Eqns. 20 and 22) are calculated for the most unstable mode for both the KH and RT instabilities. In these equations, $T_a = Oh\sqrt{We}$ is the Taylor number and $B_0 = 0.61$, $B_1 = \sqrt{3}$, $C_{RT} = 0.1$ and $C_\tau = 1$ are constants Beale and Reitz (1999).

$$\Omega_{KH} = \frac{0.34 + 0.38 We^{1.5}}{(1 + Oh)(1 + 1.4 Ta^{0.6})} \sqrt{\frac{\sigma}{\rho_g (d_p/2)^3}} \tag{19}$$

$$\Lambda_{KH} = \frac{9.02 r_p (1 + 0.45\sqrt{Oh})(1 + 0.4 Ta^{0.7})}{(1 + 0.865 We^{1.67})^{0.6}} \tag{20}$$

$$\Omega_{RT} = \sqrt{\frac{2}{3\sqrt{3\sigma}} \frac{[a_p(\rho_p - \rho_g)]^{1.5}}{\rho_p + \rho_g}} \tag{21}$$

$$K_{RT} = \sqrt{\frac{a_p(\rho_p - \rho_g)}{3\sigma}}$$
$$\Lambda_{RT} = 2\pi C_{RT}/K_{RT} \tag{22}$$

(4) The total breakup time is computed from the empirical and theoretical models.

$$\tau_{bt} = \begin{cases} 14.1We_{\delta}^{-0.25} & \text{Wert} \\ 6 & \text{Wert49} \\ \frac{5}{1-(Oh/7)} & \text{Hsiang} \\ \frac{3.726B_1 d_p}{2t_c\Omega_{KH}} & \text{KH} \\ \frac{C_\tau}{t_c\Omega_{RT}} & \text{RT} \end{cases} \tag{23}$$

(5) The representative child drop sizes for the different breakup of models are calculated as follows.

$$d_c = \begin{cases} 0.32\left[We(\tau_{b,t} - \tau_{b,i})\right]^{2/3}\frac{\sigma}{v_g^2\rho_g} & \text{Wert} \\ 0.49\left[We(\tau_{b,t} - \tau_{b,i})\right]^{2/3}\frac{\sigma}{v_g^2\rho_g} & \text{Wert49} \\ 6.2d_p\left(\frac{\rho_p}{\rho_g}\right)^{0.25}\left(\frac{\mu_p}{\rho_p d_p v_g}\right)^{0.5} & \text{Hsiang} \\ 2B_0\Lambda_{KH} & \text{KH} \\ \Lambda_{RT} & \text{RT} \end{cases} \tag{24}$$

8.6. Evaporation Models

The evaporation time is derived from the D^2 law Crowe et al. (1998) and the instantaneous droplet vaporization rate $\dot{m}_B$ proposed by Abramzon and Sirignano (1989). The evaporation time is calculated as follows:

(1) The maximum volume (when velocity equilibrium is achieved) occupied by the cloud is calculated as an ellipsoid.

$$V_{cloud} = \frac{4}{3}\pi\left(L_y\right)^2\left(L_x/2\right) \tag{25}$$

(2) The maximum vapor mass fraction possible is calculated for the droplet mass and cloud dry gas mass, m_g, using the wet bulb temperature T_{wb}, post-shock pressure P_g, and cloud volume V_{cloud}. In Eqn. 26, the subscript g denotes properties of the dry gas, v the vapor species, and m the mixture of gas and vapor. R_u is the universal gas constant The wet bulb temperature is found by solving the adiabatic saturation problem (conservation of energy at saturation).

$$m_m = m_g + m_p$$
$$Y_{vmax} = \frac{m_p}{m_m}$$
$$R_m = R_u \cdot \left[\frac{1-Y_{vmax}}{MW_g} + \frac{Y_{vmax}}{MW_v}\right] \tag{26}$$
$$P_g \cdot V_{cloud} = m_m R_m T_{wb}$$

(3) The vapor fraction in the cloud is set to the lower of Y_{vmax} and Y_{sat} the equilibrium saturation mass fraction. The Spalding mass transfer number B_M is then calculated with Y_s, the droplet surface vapor mass fraction.

$$B_M = \frac{Y_s - Y_\infty}{1 - Y_s} \tag{27}$$

(4) The film conditions for temperature and density are taken as a weighting between the free stream gas and the droplet surface conditions, where A_r is a film weighting factor taken to be 1/3 Abramzon and Sirignano (1989). In equations 28 and 29, the subscript g denotes the post-shock, free stream, and dry gas conditions, as before.

$$T_f = A_r T_g + (1 - A_r)\cdot T_p \tag{28}$$

$$\rho_f = A_r \rho_g + (1 - A_r)\cdot \rho_s \tag{29}$$

(5) From these conditions, we proceed to calculate the mass transfer rate $\dot{m}_B$, where the Sherwood number $Sh = 2$, and $\mathcal{D}_v$ is the diffusivity calculated from the Gililland model, Eqn. 30 where $/nu$ is the atomic diffusion volume for each species (see Dahal and McFarland (2017) for more).

$$MW_v = (1/MW_g + 1/MW_v)$$
$$\mathcal{D}_v = 0.0043\frac{T_f[K]^{1.5}}{P_g[atm](v_g^{1/3} + v_v^{1/3})^2}\frac{\sqrt{MW_v}}{100^2} \tag{30}$$

$$\dot{m}_B = Sh\pi d_c \rho_f \mathcal{D}_v ln(1 + B_M) \tag{31}$$

(6) The evaporation time is estimated following the D^2 law Abramzon and Sirignano (1989); Crowe et al. (1998).

$$\lambda = \frac{4}{\pi}\frac{\dot{m}_B}{\rho_p d_c} \tag{32}$$

$$t_{evp} = \frac{{d_c}^2}{\lambda} \tag{33}$$